Pergamon

Journal of the Mechanics and Physics of Solids
49 (2001) 27–68

JOURNAL OF THE
MECHANICS AND
PHYSICS OF SOLIDS

www.elsevier.com/locate/jmps

A computational model of ceramic microstructures subjected to multi-axial dynamic loading

P.D. Zavattieri, P.V. Raghuram, H.D. Espinosa *

School of Aeronautics and Astronautics, Purdue University, West Lafayette, IN 47907-1282, USA

Received 24 June 1999; received in revised form 28 March 2000

Abstract

A model is presented for the dynamic finite element analysis of ceramic microstructures subjected to multi-axial dynamic loading. This model solves an initial-boundary value problem using a multi-body contact model integrated with interface elements to simulate microcracking at grain boundaries and subsequent large sliding, opening and closing of microcracks. An explicit time integration scheme is adopted to integrate the system of spatially discretized ordinary differential equations. A systematic and parametric study of the effect of interface element parameters, grain anisotropy, stochastic distribution of interface properties, grain size and grain morphology is carried out. Numerical results are shown in terms of microcrack patterns and evolution of crack density, i.e., damage kinetics. The brittle behavior of the microstructure as the interfacial strength decreases is investigated. Crack patterns on the representative volume element vary from grains totally detached from each other to a few short cracks, nucleated at voids, except, for the case of microstructures with initial flaws. Grain elastic anisotropy seems to play an important role in microfracture presenting higher values of crack density than the isotropic case. The computational results also show that decreasing the grain size results in a decrease in crack density per unit area at equal multiaxial dynamic loading. Histograms of crack density distribution are presented for the study of the stochasticity of interface parameters. Finally, a strong dependency with grain shape is observed for different microstructures generated using Voronoi Tessellation. The micromechanical model here discussed allows the study of material pulverization upon unloading. The qualitative and quantitative results presented in this article are useful in developing more refined continuum theories on fracture properties of ceramics.

* Corresponding author. Currently at Northwestern University, Dept of Mechanical Engineering, 2145 Sheridan Road, Evanston, IL 60208-311, USA. Tel.: +1-847-467-5989; fax: +1-847-491-3915.

E-mail address: espinosa@nwu.edu, http://www.mech.nwu.edu/espinosa. (H.D. Espinosa).

0022-5096/01/$ - see front matter
PII: S0022-5096(00)00028-4

Keywords: Ceramics; A. Microstructures; C. Finite element; Fragmentation; Damage

1. Introduction

Being naturally brittle, ceramics undergo fragmentation when subjected to multiaxial loading. The shear resistance of confined ceramics plays a major role in the prevention of ballistic penetration, wear of bearings, fracture of prosthetic devices, fracture and wear of coatings, etc. Therefore, understanding the shear resistance of ceramics is important for estimating and improving their strength. It is known that investigating experimentally the behavior of ceramics is a difficult task. Moreover, experiments do not always provide direct information on crack densities and their evolution. The implementation of an iterative computational/experimental procedure requires reliable material models, physically motivated, incorporating microfailure and macrofracture at various size scales.

Attempts have been made to model the inelastic constitutive behavior of ceramics in the presence of cracks, and to validate the models through simulation of plate and rod impact experiments. Available models for the failure of ceramics are continuum damage theories (Addessio and Johnson, 1989; Curran et al., 1990; Espinosa, 1995; Johnson and Holmquist, 1992), which are based on homogenizing the cracked solid and finding its response by degrading the elasticity of the material. The fundamental assumption in these models is that the inelastic strains are caused by microcracks whose evaluation during loading degrades the strength of the material. This degradation is defined in terms of reduced moduli whose evaluation under compressive, as well as tensile loading, is formulated using the generalized Griffith criterion. In addition, some of these models account for the initiation of cracks, coalescence, friction between fragments in the comminuted zone, etc. However, some of these phenomenological models cannot describe damage induced anisotropy, their parameters are difficult to measure experimentally, and do not explicitly consider the discrete nature of fracture through crack growth and coalescence.

In spite of the above developments, continuum models have been criticized because they require assumptions on the size and distribution of microcracks to start with, and because they cannot describe the growth of dominant cracks leading to failure, which are not suitable to homogenization. Models based on a discrete approach (Camacho and Ortiz, 1996; Espinosa et al., 1998b; Miller et al., 1999; Xu and Needleman, 1995; etc.) nucleate cracks, and follow their propagation and coalescence during the deformation process. This is a phenomenological framework where the fracture characteristics of the material are embedded in a cohesive surface traction-displacement relation.

During the last few years, the mechanical behavior of polycrystalline ceramics has been studied quite extensively on a microstructural base. The influence of microscopic heterogeneities on the overall behavior, depends on morphological characteristics such as size, shape, lattice orientation and spatial distribution of different material properties. In our view, the calculation of stress and strain distributions in

real and idealized microstructures can increase the understanding of the different mechanisms that control macroscopic response. Furthermore, these micromechanical simulations can be useful for quantification and determination of failure mechanisms, as well as the derivation of evolution equations to be used in continuum models, (Curran et al., 1990; Espinosa, 1995; Espinosa et al., 1998b). In this way, bridging between length scales can be accomplished.

In the case of metal–matrix composites, Ghosh and Yunshan (1995) and Ghosh et al. (1997) developed a material based *Voronoi Cell Finite Element Model* (VCFEM) in an attempt to overcome difficulties in modeling arbitrary microstructures by conventional finite element methods. Voronoi cells are utilized to obtain stereologic information for the different morphologies. The microscopic analysis is conducted with the Voronoi cell finite element model while a conventional displacement based FEM code executes the macroscopic analysis. This method has been tested in several heterogeneous microstructures. Discrete microcracking was not explicitly included in this model.

Onck and Van der Giessen (1999) proposed a microstructurally-based modeling technique to study the intergranular creep failure of polycrystals by means of *grain elements*. A crack tip process zone was used in which grains and their grain boundaries were represented discretely, while the surrounding undamaged material was described as a continuum. The constitutive description of tile grain boundaries accounted for the relevant physical mechanisms, i.e. viscous grain boundary sliding, the nucleation and growth of grain boundary cavities, and microcracking by the coalescence of cavities. Discrete propagation of the main crack occurred by linking up of neighboring facet microcracks.

Wu and Niu (1995a,b) presented a micromechanical model of the fracture of polycrystalline ice. Their model is based on a statistical description of the ice microstructure, which contains crystals of random sizes and orientations and a random distribution of grain boundary crack precursors. The analysis takes into account microstructural stresses originating from the elastic anisotropy of the constituent crystals. Friction in precursors and crack–crack interactions are also considered. The model is applied to several microstructures generated from a graph model. It was shown that the critical crack density, and critical damage, were not appropriate descriptors of failure, that the compressive strength was strongly dependent, on the microstructural variations and that crack–crack interactions were very important in compressive fracture.

Kim et al. (1996) studied crack propagation in alumina ceramics. The competition between intergranular and transgranular propagation was utilized to determine the crack path.

Miller et al. (1999) considered models based on energy balance and compared their predictions of fragment size to the results of numerical simulations. They found differences due to the fact that the energy-based models deal with the onset of the fragmentation event, but they do not include the time dependence of the process. Therefore, they proposed a model that included the time history of the fragmentation process and parameters such as the speed of crack propagation, and the strength and flaw distribution.

In this paper, a micro-mechanical finite element, modeling of ceramic microstructures under dynamic loading is presented to assess intergranular microcrack initiation and evolution. A representative volume element of an actual microstructure, subjected to compression–shear dynamic loading, is considered for the analysis. A large deformation elastic–anisotropic viscoplasticity model for the grains, incorporating grain anisotropy by randomly generating principal material directions, is included. Cohesive interface elements are embedded along grain boundaries to simulate microcrack initiation and evolution. Their interaction and coalescence are a natural outcome of the calculated material response.

A systematic and parametric study of the effect of different factors is carried out. The effects of interface element parameters, grain anisotropy, grain size and a stochastic distribution of interface properties are studied in terms of microcrack initiation and evolution and crack density. The pulverization of the material upon unloading is examined with the microstructural model. The qualitative and quantitative results presented in this article are intended to provide valuable insight for developing more refined continuum theories on fracture properties of ceramics.

2. Computational model

The finite element analysis of the initial boundary value problem is performed using a total Lagrangian continuum approach with a large deformation elastic–anisotropic model.

A displacement based finite element formulation is obtained from the weak form of the momentum balance or dynamic principle of virtual work. The weak form at time t in total Lagrangian co-ordinates, (i.e., referred to the reference configuration), is given by

$$\int_{B_0} [\nabla_0 \mathbf{T}^0 + \rho_0(\mathbf{b}_0 - \mathbf{a})] \cdot \eta \, dB_0 = 0 \tag{1}$$

$$\int_{B_0} \mathbf{T}^0 : \nabla_0 \eta \, dB_0 - \int_{B_0} \rho_0(\mathbf{b}_0 - \mathbf{a}) \cdot \eta \, dB_0 - \int_{S_{0\sigma}} \mathbf{t} \cdot \eta \, dS_0 = 0 \tag{2}$$

where $\mathbf{T}^0$ is the first, Piola–Kirchhoff stress tensor at time t; $\mathbf{b}_0$, $\mathbf{a}$, and $\mathbf{t}$ are the body force vector, acceleration vector, and boundary traction vector on volume B_0, and boundary $S_{0\sigma}$, respectively. Virtual displacement field η is assumed to be admissible, and ρ_0 represents the material density per unit, volume in the reference configuration. The symbol ∇_0 denotes the material gradient with respect to the reference configuration, and ":" is used to denote the inner product between second order tensors, e.g., $\mathbf{A}:\mathbf{B} \equiv A_{ij}B_{ji}$, where the summation convention on repeated indices is implied.

Alternately, the weak form of the momentum balance, in terms of spatial quantities, is given by

$$\int_{B_0} \tau : \nabla^s \eta \, dB_0 - \int_{B_0} \rho_0 (\mathbf{b}_0 - \mathbf{a}) \cdot \eta \, dB_0 - \int_{S_{0\sigma}} \mathbf{t} \cdot \eta \, dS_0 = 0 \tag{3}$$

in which superscript s stands for the symmetric part of the tensor, $\tau = \mathbf{F}\mathbf{T}^0$ is the Kirchhoff stress, $\mathbf{F}$ is the deformation gradient at time t, and ∇ is the spatial deformation tensor. As Eq. (3) shows, the equation of motion in its weak form states that the work done by the stresses τ over strains $\nabla^s \eta$ equals the work done by applied body forces, inertia forces, and surface tractions.

In the absence of body forces, substitution of the discretized variables into Eq. (3) leads to the following system of ordinary differential equations. The above equation can be written at time t for explicit integration as,

$$\mathbf{M}\mathbf{a} = \mathbf{f}_{ext} - \mathbf{f}_{\text{int}} \tag{4}$$

where $\mathbf{M}$ is the lumped mass matrix, $\mathbf{a}$ is the global acceleration vector and $\mathbf{f}_{\mathbf{ext}}$ and $\mathbf{f}_{\mathbf{int}}$ are the external and internal force vectors. In order to obtain a uniform mass distribution in the mesh, the element mass was lumped proportional to the angles formed by the corner nodes and midnodes, as detailed in Espinosa et al. (1998b).

2.1. Anisotropic elastic model

An elastic–anisotropic model is used to describe the grains single crystal behavior. The second Piola–Kirchhoff stress tensor relative to the underformed configuration is described by

$$\mathbf{S}_{ij} = C_{ijkl} \mathbf{H}_{kl} \tag{5}$$

Where $\mathbf{H} = \frac{1}{2} \ln C$ is a logarithmic strain measure or Henky strain, $\mathbf{C} = \mathbf{F}\mathbf{F}^{\mathrm{T}}$ is the elastic right Cauchy–Green deformation tensor, and C_{ijkl} is the elastic anisotropic material stiffness tensor in the global co-ordinates (x,y,z).

In the case of anisotropic crystals, the elastic constitutive matrix $\hat{C}_{IJKL}$ is defined in the local co-ordinate system of the grain by its principal material directions (1,2,3), such that $C_{ijkl} = \mathbf{T}^c_{iI} \mathbf{T}^c_{jJ} \mathbf{T}^c_{kK} \mathbf{T}^c_{lL} \hat{C}_{IJKL}$, where $\mathbf{T}^c$ is the transformation matrix.

Each grain is assumed to be elastic orthotropic and the orientation of the principal material directions differs from grain to grain. In order to keep the plane strain condition in the x-y plane, one of the principal material directions has to coincide with the z-axis. Therefore, three cases are considered randomly for each grain, Case 1: $1 \equiv z$, Case 2: $2 \equiv z$ or Case 3: $3 \equiv z$ (see Fig. 1). The angle between the global axes x, y, and the two local axes lying in the plane x-y is also generated randomly. The grain local axes and the corresponding analysis global axes are shown in Fig. 2. In general, this approach could be used for any orthotropic materials where the normal to the three symmetry planes coincides with the local axes of co-ordinates. i.e. tetragonal systems: Indium, Tin, Zircon; transversely isotropic systems: Cadmium, Ice, Zinc; cubic: Aluminum, Copper, Nickel, etc.

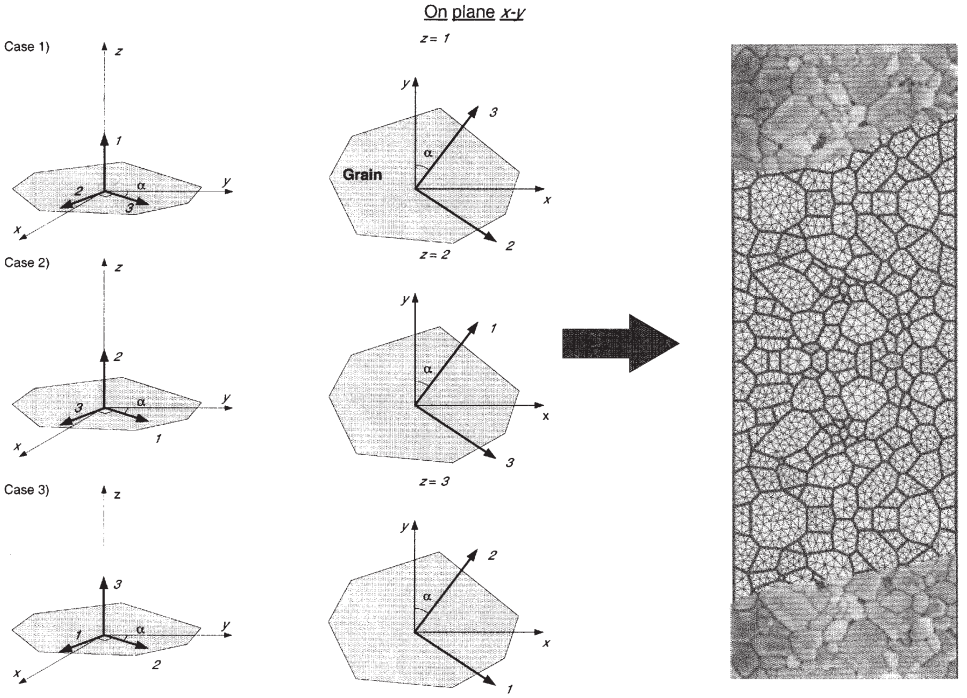

Fig. 1. Description of the principal material directions (1, 2, 3) of each grain relative to the global coordinates of the overall microstructure (x, y, z). Actual picture of the microstructure utilized for the FEM analysis where each grain is represented by a six-noded triangular mesh.

2.2. Contact/interface algorithm

A multi-body contact-interface algorithm to describe the kinematics at the grain boundaries is used to simulate crack initiation and propagation, Espinosa et al. (1998a,b, 2000). An explicit time integration scheme is adapted to integrate the system of spatially discretized ordinary differential equations. Fig. 3 describes the contact model which is integrated with interface elements to simulate microcracking at the grain boundaries and subsequent large sliding, opening and closing of the interface. The tensile and shear tractions in the zero thickness interface elements, embedded along grain boundaries, are calculated from the interface cohesive law. The interface cohesive law describes the evolution of these tractions in terms of both normal and tangential displacement jumps. Within the framework of cohesive interface elements the two most noteworthy cohesive failure models available in the literature are the potential-based law used by Tvergaard (1990) and Xu and Needleman (1995), and the linear law developed by Camacho and Ortiz (1996) and Ortiz and Pandolfi (1999).

The model presented in this paper is based on the interface model proposed by Espinosa et al. (2000b) for dynamic calculations. It assumes that the interface carries forces that oppose separation and shear between two surfaces until debonding. The

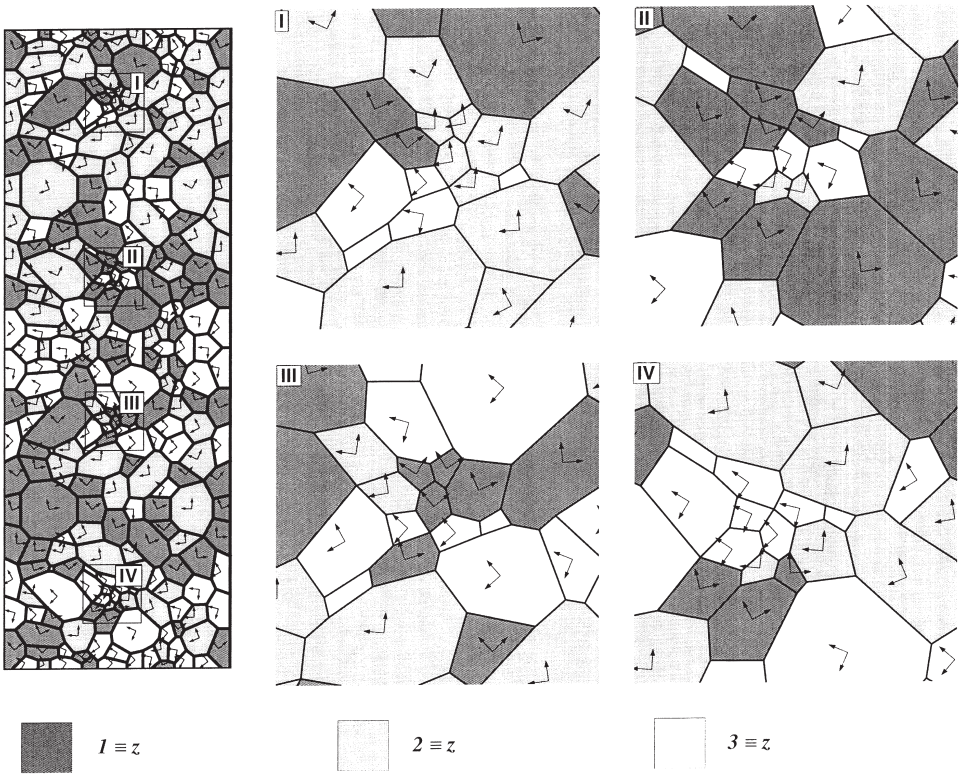

Fig. 2. Distribution of the principal material directions. Different intensities of gray indicate which principal direction coincides with the global z axis. The local system of co-ordinates in the x–y plane is represented by two vectors.

magnitude of these forces is a function of the relative separation and shear displacements between the two surfaces. The compressive tractions at the grain boundaries are calculated through the impenetrability condition employed in the contact model. The interface between two bodies is intact until the interface traction reaches the maximum value. Once the maximum traction is reached, the interface starts failing and the traction reduces to zero linearly up to the maximum displacement jump.

Following Camacho and Ortiz (1996) and Ortiz and Pandolfi (1999), in formulating the cohesive law, a non-dimensional effective displacement jump is defined by

$$\lambda = \sqrt{\left(\frac{u_n}{\delta_n}\right)^2 + \beta^2\left(\frac{u_t}{\delta_t}\right)^2} \tag{6}$$

where, u_n and u_t are the actual normal and tangential displacement jumps at the interface estimated by the finite element, analysis, and δ_n and δ_t are critical values at which interface failure takes place.

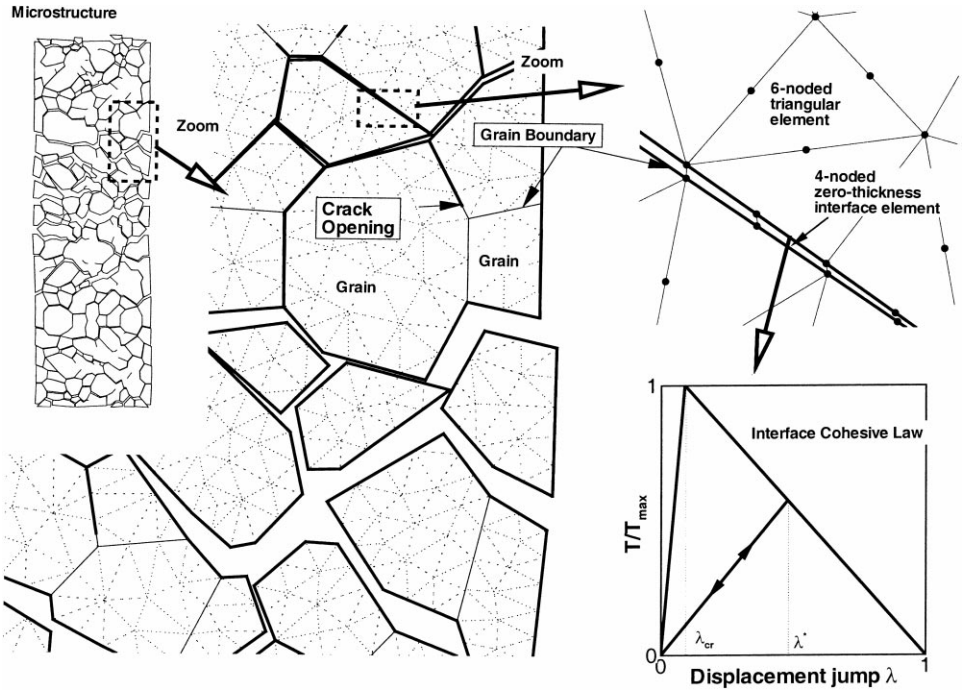

Fig. 3. Schematics of microcracking at grain boundaries using the irreversible interface cohesive law. Evolution of the traction with loading and unloading is also shown.

For a triangular T-λ law, see Fig. 3, loading and unloading in the range $0 \leq \lambda \leq \lambda_{cr}$ are given by

$$T_n = \frac{u_n T_{\max}}{\delta_n \lambda_{cr}}; \; T_t = \alpha \frac{u_t T_{\max}}{\delta_t \lambda_{cr}} \tag{7}$$

$T_{\max}$ is the maximum normal traction that the interface can develop before failure and $\alpha = \beta\left(\frac{\delta_n}{\delta_t}\right)$ is the parameter coupling the normal and shear tractions, such that $\beta^2 = G_{IIc}/G_{Ic}$.

It is assumed here that the traction can increase reversible and linearly to its maximum value $T = T_{\max}$ when $\lambda = \lambda_{cr}$. Beyond λ_{cr}, the traction reduces to zero up to $\lambda = 1.0$ and any unloading takes place irreversibly, see Camacho and Ortiz (1996) and Ortiz and Pandolfi (1999).

For loading in the range $\lambda_{cr} < \lambda \leq 1$;

$$T_n = T_{\max} \frac{u_n \quad 1-\lambda}{\delta_n \lambda (1-\lambda_{cr})}; \; T_t = \alpha T_{\max} \frac{u_t \quad 1-\lambda}{\delta_t \lambda (1-\lambda_{cr})}. \tag{8}$$

Due to irreversibility, loading/unloading in the range $0 \le \lambda \le \lambda^*$, where $\lambda^* > \lambda_{cr}$ is the last value of λ from where unloading took place, is given by

$$T_n = \frac{u_n T_{\max}}{\delta_n \ \lambda^*}; \ T_t = \alpha \frac{u_t T_{\max}}{\delta_t \ \lambda^*} \tag{9}$$

For loading in the range $\lambda^* < \lambda \le 1$;

$$T_n = T_{\max} \frac{u_n \quad 1-\lambda}{\delta_n \lambda (1-\lambda^*)}; \ T_t = \alpha T_{\max} \frac{u_t \quad 1-\lambda}{\delta_t \lambda (1-\lambda^*)}. \tag{10}$$

Once the effective displacement jump reaches or exceeds a value of 1, the interface element is assumed to have failed and microcracking is said to have initiated at that grain boundary. Subsequent failure of neighboring interface elements leads to microcrack propagation and coalescence. In our graphic representation, failed interface elements are represented with thicker lines.

From the values of fracture toughness K_{IC}, or equivalently G_{IC}, assuming plane strain, and the maximum interface stress, the critical interface displacement jump is computed by equating the area under the T-δ diagram to G_{IC}, namely,

$$G_{\mathrm{IC}} = \frac{1}{2} \delta_n T_{\max} \tag{11}$$

The slope of the curve in Fig. 3 going from 0 to λ_{cr}, $\mathbf{s} = T_{\max}/(\lambda_{cr}\delta)$, is selected such that the wave speed in the material with interfaces is the same as the ones in the material without interfaces during reversible loading.

In contrast with the standard explicit schemes, where the time steps are limited by stability in order to ensure that waves do not propagate through the mesh faster than the material wave speed, this algorithm considers an additional limitation in the time step controlled by the cohesive law.

As it can be seen in Fig. 3, the cohesive interface law consists only of two parts $0 \le \lambda < \lambda_{cr}$ and $\lambda_{cr} \le \lambda \le 1$. The time step has to be such that the evolution of λ can follow the cohesive law curve in several time steps. This is accomplished by taking

$$\Delta t_{\mathrm{cohesive}} = \frac{\Delta t_{\mathrm{continuum}} \cdot F}{\max_i \zeta_i} \tag{12}$$

where ξ_i is defined by each interface element, i as:

$$\zeta_i = \begin{cases} \dfrac{\Delta\lambda}{\lambda_{cr}} & \text{if } 0 \le \lambda < \lambda_{cr} \\ \dfrac{\Delta\lambda}{1-\lambda_{cr}} & \text{if } \lambda_{cr} \le \lambda < 1 \end{cases} \tag{13}$$

In the above equation $\Delta\lambda = \hat{\lambda}_{n+1} - \lambda_n$ where $\hat{\lambda}_{n+1}$ is the displacement jump predictor

for interface i. F is the inverse of the number of steps required for λ to go from 0 to λ_{cr}.

In this way, the overall time step is taken as

$$\Delta t = \min(\Delta t_{\text{cohesive}}, \Delta t_{\text{continuum}}) \tag{14}$$

where $\Delta t_{\text{continuum}}$ is the stable time step calculated from the maximum six-noded element, frequency in the mesh $\omega_{\max}$ (Espinosa et al., 1998a).

One of the limitations of the contact/interface algorithm is that it is very susceptible to instabilities if the time step changes suddenly. As mentioned before, the time step is controlled by the variation in time of the interface element displacement jump, $\dot{\lambda}$, which can change suddenly from one step to another for more than one order of magnitude depending on the contact conditions of the interface element. This may lead to numerical instabilities unless precautions are taken. In order to avoid these instabilities, each element (six-noded and interface elements) is advanced in time with the Δt computed by Eq. (14), while the contact algorithm is advanced in time with $\Delta t_{\text{continnum}}$.

Considering that the multi-body contact algorithm is one of the most, time consuming parts of the micromechanical model, it can be said that this subcycling algorithm not only solves stability problems, but also can provide some speed up in the calculation.

2.3. Grain discretization

The micromechanical model is based on a plane strain analysis of a polycrystalline material which is described with a multi-body finite element mesh. Each grain is individually represented by a mesh with six-noded triangular finite elements, generated using Delaunay triangulations and four-noded interface elements inserted at the grain boundary.

A real ceramic microstructure is digitized to represent the grain morphology as shown in Fig. 1. After digitalization, the grain boundaries are represented by polygons and a mesh is generated inside each polygon using triangular elements and interface elements along the edges in such a way that the nodes belonging to the interface elements are the nodes of the triangular elements on the polygon boundaries.

Each grain is described by its principal material directions relative to the global co-ordinates. The distribution of the principal material directions on the overall microstructure can be seen in Fig. 2. The angle between local and global co-ordinates for each grain is obtained by means of a random number generation routine.

2.4. Summary of the explicit integration algorithm

An explicit central-difference integration algorithm is being used to integrate the system of spatially discretized ordinary differential equations in time. The algorithm, accounting for acceleration corrections due to contact, is summarized in Table 1. As in any initial boundary value problem, initial displacements and velocities $\mathbf{u}^0$ and $\mathbf{v}^0$

Table 1
Explicit integration algorithm

1. Initial conditions:

$$t = 0 \quad t_{contact} = 0 \quad n = 0$$

$$\mathbf{u}_o = \overline{\mathbf{u}}_o \quad \mathbf{v}_o = \overline{\mathbf{v}}_o \quad \mathbf{t}_o = \overline{\mathbf{t}}_o$$

$$\mathbf{a}_o = (\mathbf{f}_o^{ext} - \mathbf{f}_o^{int})/\mathbf{M} \quad \Rightarrow \quad \text{Where} \quad \begin{cases} \mathbf{f}_o^{int} = \int_{B_o} \mathbf{B}^T \tau_o dB_o & \text{for elements} \\ \mathbf{f}_o^{ext} = -\text{Area}(\rho c)_f \mathbf{v}_o & \text{for viscous BCs} \\ \mathbf{f}_o^{ext} = \int_{S'} N_s^T T dS' & \text{for interface elements} \end{cases}$$

2. Compute $\Delta t = \min(\Delta t_{cohesive}, \Delta t_{continuum})$

$$\begin{cases} \Delta t_{continuum} < 2/\omega_{max} & \text{for triangular elements} \\ \Delta t_{cohesive} & \text{for interface elements} \end{cases}$$

$t = t + \Delta t$

3. Correct accelerations due to changes in boundary conditions:

$$\mathbf{a}_n = \mathbf{a}_n + \frac{\mathbf{t}_{n+1} - \mathbf{t}_n}{\mathbf{M}} \qquad @ \text{ unloading}$$

4. Compute displacement predictor:

$$\begin{cases} \hat{\mathbf{u}}_{n+1} = \mathbf{u}_n + \Delta t \mathbf{v}_n + \frac{1}{2}\Delta t^2 \mathbf{a}_n & \text{for elements} \\ \hat{\mathbf{u}}_{n+1} = \mathbf{u}_n + \Delta t \mathbf{v}_n + \frac{1}{2}\Delta t^2 \left(\mathbf{a}_n - \frac{\text{Area}(\rho c)_f (\mathbf{v}_n - \mathbf{v}_{n-1})}{\mathbf{M}}\right) & \text{for viscous BCs} \end{cases}$$

5.

$\boxed{\text{If } t \geq t_{contact} + \Delta t_{continuum}}$ $\Rightarrow$ compute $\Delta \mathbf{a}_n$ (Correction of the accelerations due to contact)

The forces on the slave nodes are computed with the time step $\Delta t_{contact} = t - t_{contact}$.

$t_{contact} = t$

$\boxed{\text{Otherwise}}$

$\Delta \mathbf{a}_n = 0$

6. Update displacements:

$$\begin{cases} \mathbf{u}_{n+1} = \mathbf{u}_n + \Delta t \mathbf{v}_n + \frac{1}{2}\Delta t^2 \mathbf{a}_n + \frac{1}{2}\Delta t_{contact}^2 \Delta \mathbf{a}_n & \text{for elements} \\ \mathbf{u}_{n+1} = \mathbf{u}_n + \Delta t \mathbf{v}_n + \frac{1}{2}\Delta t^2 \left(\mathbf{a}_n - \frac{\text{Area}(\rho c)_f (\mathbf{v}_n - \mathbf{v}_{n-1})}{\mathbf{M}}\right) + \frac{1}{2}\Delta t_{contact}^2 \Delta \mathbf{a}_n & \text{for viscous BCs} \end{cases}$$

7. Impose periodic boundary conditions on the displacements $\mathbf{u}_{n+1}$.
8. Update $\overline{\mathbf{S}} = \overline{\mathbf{S}}(\mathbf{u}_{n+1})$ and compute internal force vector:

$$\begin{cases} \mathbf{f}_{n+1}^{int} = \int_{B_o} \mathbf{B}^T \tau_{n+1} dB_o & \text{for elements} \\ \mathbf{f}_{n+1}^{ext} = -\text{Area}(\rho c)_f \mathbf{v}_n & \text{for viscous BCs} \\ \mathbf{f}_{n+1}^{ext} = \int_{S'} N_s^T T dS' & \text{for interface elements} \end{cases}$$

9. Solve for accelerations:

$$\mathbf{a}_{n+1} = (\mathbf{f}_{n+1}^{ext} - \mathbf{f}_{n+1}^{int})/\mathbf{M}$$

10. Update velocity vector:

$$\begin{cases} \mathbf{v}_{n+1} = \mathbf{v}_n + \frac{\Delta t}{2}(\mathbf{a}_n + \mathbf{a}_{n+1}) + \frac{1}{2}\Delta t_{contact} \Delta \mathbf{a}_n & \text{for elements} \\ \mathbf{v}_{n+1} = \mathbf{v}_n + \frac{\Delta t}{2}(\mathbf{a}_n + \mathbf{a}_{n+1} - \frac{\text{Area}(\rho c)_f (\mathbf{v}_n - \mathbf{v}_{n-1})}{\mathbf{M}}) + \frac{1}{2}\Delta t_{contact} \Delta \mathbf{a}_n & \text{for viscous BCs} \end{cases}$$

11. Impose periodic boundary conditions on the velocities $\mathbf{v}_{n+1}$.
12. $n = n + 1$, if $n < n_{max}$ go to step (2), else stop.

are required. Initial accelerations $\mathbf{a}_0$ are calculated from initial applied forces $\mathbf{f}_0^{\text{ext}}$ and initial internal forces $\mathbf{f}_0^{\text{int}}$.

At each time step n, the nodal accelerations must first be corrected for any time-dependent changes in the traction boundary conditions. Then, a displacement predictor at time n+1 is computed using the corrected acceleration and the displacements and velocities at time step n. Modified accelerations at time n, $\Delta\mathbf{a}_n$, are computed based on the corrected acceleration and changes in accelerations resulting from surface contact determined from the displacement predictor at n+1. Updated displacements at n+1 are used in the update of stresses and the computation of internal forces. In contrast with the original algorithm presented by Espinosa et al. (1998a), the correction of the accelerations is multiplied by a different time step ($\Delta t_{\text{contact}}$) described in Section 2.2. Lastly, accelerations and velocities at time n+1 are obtained completing the time integration scheme. Corrected accelerations at step (3) need to be computed. These correction terms arise from changes in the applied boundary traction due to changes in the applied external forces, (Espinosa et al., 1992). If such corrections are not incorporated in the numerical implementation, spurious oscillations are introduced with magnitudes proportional to the traction change.

3. Case study: pressure–shear experiment

Plate impact experiments offer unique capabilities for the characterization of advanced materials under dynamic loading conditions. These experiments allow high stresses, high pressures, high strain rates and finite deformations to be generated under well characterized conditions. They all rely on the generation of one-dimensional waves in the central region of the specimen in order to allow a clear interpretation of the experimental results and the mathematical modeling of the material behavior. Compression–shear loading is attained by inclining the flyer, specimen, and target plates with respect to the axis of the projectile (Clifton and Klopp, 1985). By varying the angle of inclination, a variety of loading states may be achieved. Pressure shear recovery experiments offer several advantages over other experimental techniques in the study of damage and inelasticity in advanced materials (Espinosa et al., 2000a). The stress amplitudes and deformation rates obtained in these experiments allow the identification of damage and material instabilities.

Furthermore, the information gathered from these experiments can be substantially increased by correlation of real-time velocity profiles and microstructural features associated with mechanisms of inelasticity and damage. Ceramics are so susceptible to fragmentation that they can pulverize upon unloading if enough damage and elastic energy is stored within the material in the loading phase. This makes the recovery of samples very difficult in experiments. Our goal is to simulate the pressure–shear experiment, performed by Espinosa et al. (2000a) to demonstrate the onset of various failure mechanisms and their evolution.

3.1. Boundary and initial conditions

Fig. 4 shows the pressure–shear configuration. The specimen is a thin wafer of 540 μm, sandwiched between two anvil plates, i.e. the flyer and the target. In this configuration, the flyer hits the specimen, which is attached to the target, with an initial velocity V_0=148 m/s. The angle of inclination in this case is γ=18°. The impactor is glued to the front end of a fiberglass tube with the impact plane skewed from the axis of the tube at the desired angle.

At impact, plane compression waves and shear waves are produced in both the impactor and the target. Since the shear wave velocity is approximately half the longitudinal wave velocity, a thin film with very low shear resistance needs to be added to the flyer plate such that the arrival of the unloading shear wave to the impact surface precedes the arrival of the unloading longitudinal wave generated at the back surface of the second flyer plate. Certainly, the thickness of the anvil or target plate must be selected such that the arrival of longitudinal unloading to the impactor surface, from the anvil back surface, does not prevent the transfer of the main pulses to the target plate.

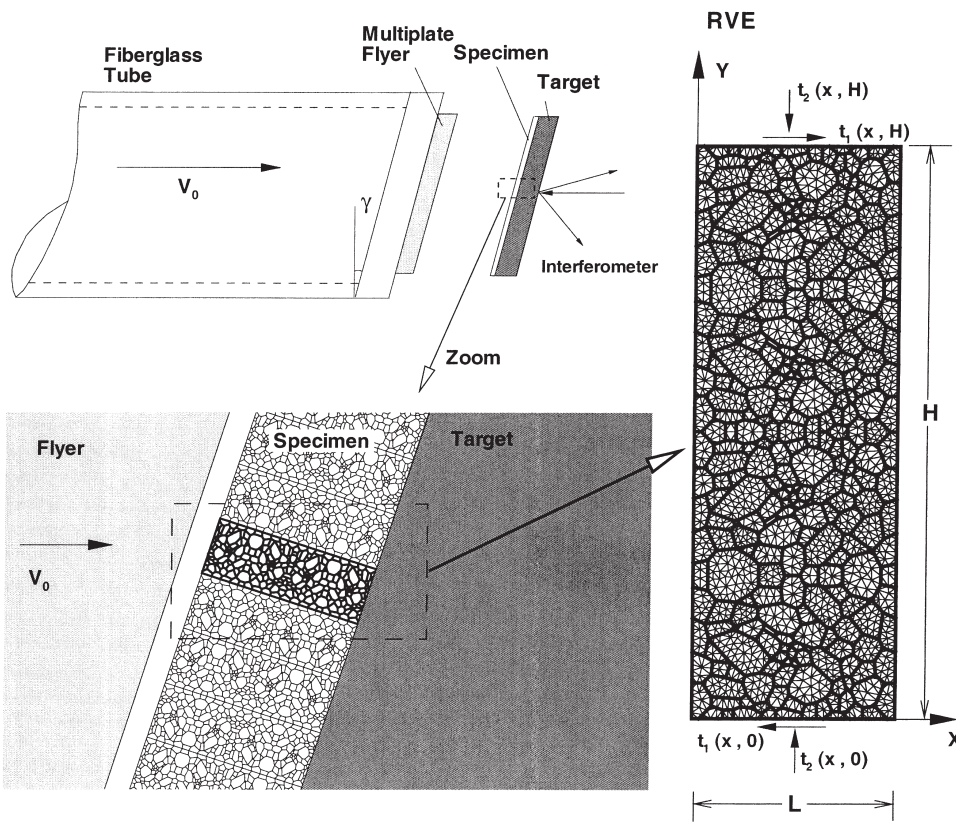

Fig. 4. Schematics of the experimental configuration and the representative volume element.

For a microstructural analysis of the pressure–shear configuration (as shown in Fig. 4), a representative volume element is selected. The flyer–specimen interface is located at $y=H$, while the specimen–target interface is at $y=0$. Assuming that the computational cell is repeated in the x-direction, the following periodic boundary conditions are applied

$$\mathbf{u}(0,y,t)=\mathbf{u}(L,y,t)\quad \mathbf{v}(0,y,t)=\mathbf{v}(L,y,t)\quad \mathbf{a}(0,y,t)=\mathbf{a}(L,y,t) \tag{15}$$

where **u**, **v** and **a** are the displacement, velocity and acceleration vector fields. Grains with nodes at $x=0$ have the same principal material directions as the grain with nodes at $x=L$ in order to ensure periodicity. In addition, the condition of uniform **u**, **v** and **a** at the flyer–specimen and specimen–target interfaces is imposed by averaging the quantities at the top and bottom nodes of the specimen. Furthermore, assuming that the target and flyer plates remain elastic throughout the deformation process, the computational effort can be minimized by replacing the flyer and anvil plates with viscous boundary conditions based on one dimensional elastic wave theory (Espinosa et al., 1992; Zhou et al., 1994). This implies the assumption that the flyer and anvil plates do not have any relative sliding. Conservation of momentum and continuity of velocities and tractions lead to the following equations for tractions t_1 and t_2 at, $y=H$ and $y=0$.

$$t_1(x,H,t)=-(\rho c_s)_f[v_1(x,H,t)-v_1^0] \tag{16}$$

$$t_2(x,H,t)=-(\rho c_l)_f[v_2(x,H,t)-v_2^0] \tag{17}$$

$$t_1(x,0,t)=-(\rho c_s)_t v_1(x,0,t) \tag{18}$$

$$t_2(x,0,t)=-(\rho c_l)_t v_2(x,0,t) \tag{19}$$

where $()_f$ and $()_t$ denote flyer and target quantities, c_l and c_s are longitudinal and shear wave speeds, ρ is the specific material density, v_1 and v_2 are in-plane and normal velocities and v_1^0 and v_2^0 are the in-plane and normal velocities of the flyer plate. The flyer shear and normal velocities are obtained from the projectile velocity, V_0 and pressure shear angle γ as

$$v_1^0=V_0\sin\gamma\quad v_2^0=V_0\cos\gamma \tag{20}$$

The initial in-plane and normal velocities at the specimen–target interface are zero and at the flyer–specimen interface they are given by

$$v_1(x,H,0)=\frac{(\rho c_s)_f}{(\rho c_s)_s+(\rho c_s)_f}v_1^0 \tag{21}$$

$$v_2(x,H,0)=\frac{(\rho c_l)_f}{(\rho c_l)_s+(\rho c_l)_f}v_2^0 \tag{22}$$

in which $(\rho c_s)_s$ and $(\rho c_l)_s$ are the shear and longitudinal impedances of the specimen.

The material properties of the ceramic specimen (Al_2O_3/SiC nanocomposite), longitudinal and shear impedances of the steel flyer and target plates are given in

Table 2. In tile case of the ceramic, the nonzero components are denoted by only two indices (i.e. $C_{1111}=C_{11}$, $C_{2222}=C_{22}$, $C_{1122}=C_{12}$, $C_{1212}=C_{44}$, etc). It should be pointed out that alumina is a trigonal system with only three planes of symmetry with normals that do not coincide with the local axes of co-ordinates except for axis 1. In terms of the elastic constitutive matrix $\hat{C}_{IJ}$, this means that $C_{14}=-C_{24}=C_{45}\neq 0$ (Hearmon, 1956). In order to address this problem the authors assumed the behavior of the alumina to be transversely isotropic (or hexagonal) making $C_{14}=0$. It is demonstrated in Section 4.5.1 that the effect of using this approximation is not significant in the response of the microstructure.

4. Results and discussion

We shall focus on the study of the variation of geometrical and physical parameters that characterize the ceramic microstructure and their effect on the microstructure response.

In principle, the response of the piece of ceramic considered may depend on sev-

Table 2
Material Properties

Specimen Properties	Al_2O_3/Sic
Elastic:	
Young's Modulus E	384.6 GPa
Poisson's ratio ν	0.237
Density ρ	4000 kg/m^3
Longitudinal Wavespread C_l	10 560 m/s
Shear Wavespread C_s	6240 m/s
Longitudinal Impedance $(\rho C_l)_s$	$42.24\frac{\text{GPa}}{\text{mm}/\mu\text{sec}}$
Shear Impedance $(\rho C_s)_s$	$24.96\frac{\text{GPa}}{\text{mm}/\mu\text{sec}}$
Anisotropic Elastic Constant	Hearmon (1956)
$C_{11}=C_{22}$	465 GPa
C_{12}	124 GPa
$C_{13}=C_{23}$	117 GPa
C_{33}	563 GPa
$C_{44}=\frac{1}{2}(C_{11}-C_{12})$	
$C_{55}=C_{66}$	233 GPa
Flyer/Target Properties	Hampden Steel
Longitudinal Impedance ρC_l	$47.62\frac{\text{GPa}}{\text{mm}/\mu\text{sec}}$
Shear Impedance ρC_s	$25.46\frac{\text{GPa}}{\text{mm}/\mu\text{sec}}$

eral factors such as grain anisotropy, interfacial strength, representative computational cell size, shape and size of the grains, etc.

In order to validate our model, microstructure response should not depend on numerical parameters such as element, size, interface element length, etc. There are also some other factors that need to be properly calibrated such as the slope of the cohesive law **s**, and F, which have been described in Section 2.2. All these parameters have been successfully obtained and tested but not presented in this paper.

The first result presented in this section describes microcrack evolution and coalescence in terms of crack pattern and crack density. After that, a systematic and parametric study of the effect of factors that control the microstructure response is reported.

4.1. Microcrack evolution and material pulverization

The representative volume element presented in Figs. 1 and 4 under the dynamic conditions described in Section 3.1 is simulated using the material parameters given in Table 2, while the interfacial strength parameters are defined as K_{IC}=4 MPa·m$^{1/2}$ and T_{max}=1 GPa. Other interface parameters are β=1, α=1 and δ_t=δ_n=0.01418 μm.

Fig. 5 shows the evolution of the crack pattern along the whole microstructure. As the wave front, advances, crack nucleation and growth occur up to the moment when the wave reaches the bottom face. As described earlier, once the effective displacement jump exceeds a value of 1, the interface elements are assumed to have failed and a microcrack is said to have initiated at that grain boundary. As all grain boundaries are embedded with interface elements, the lines shown in Fig. 5 indicate the boundary of the grains that have failed during loading. Subsequent failure of neighboring interface elements leads to microcrack propagation and coalescence. As it can be observed in Fig. 5, the majority of microcracking occurs at the initial loading phase, from 0 to 100 nanoseconds. The saturation of microcracking can be noticed in the subsequent loading phase, from 100 to 500 nanoseconds during which residual stresses start building up in the specimen.

Although crack patterns provide understanding of the process of microfracture inside the ceramic, the use of stereology provides more insight of the different damage mechanisms.

Quantitative stereology attempts to characterize numerically geometrical aspects of the microstructure of interest. Underwood (1970), presented a technique to estrapolate from 2-D crack lines to 3-D complex crack surfaces. The technique provides an estimate of microcrack surface area per unit volume, S_v. By equating the total crack surface area per unit volume, S_v, to twice the average value of the number of intersections of a set of test, lines of unit, length P_L, an estimate of S_v can be obtained. P_L is the number of intersections/(Number of lines×Length of each line/Magnification). For anisotropic microstructures, the number of intersections of a set of test lines, with the boundaries of microcracks, depends on the angular orientation of the test lines in the plane. Thus, in order to obtain a representative average value of the intersection count, it is important to perform the measurements on different angular orientations in the cross-section under interrogation. The dependence of

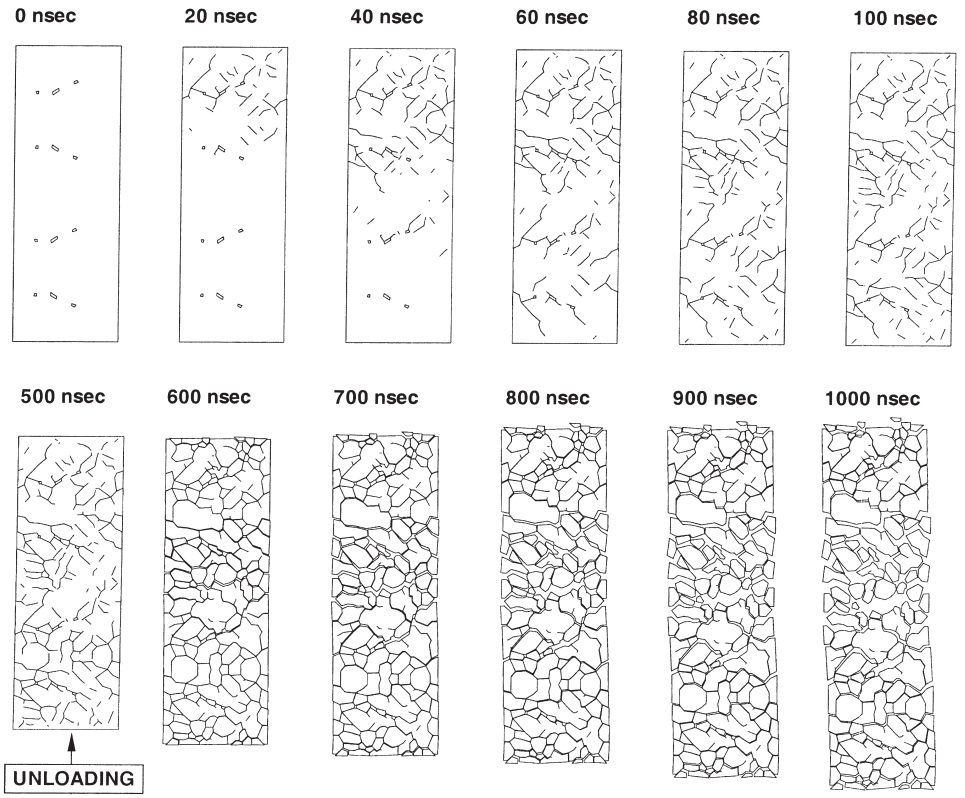

Fig. 5. Crack pattern evolution for the first 100 nanoseconds and material pulverization after 500 nanoseconds.

the number of intersections per unit length with the angle of the test lines can be used to characterize the degree of microcracking anisotropy.

For the case of our numerical simulations, the microcrack surface area per unit volume is directly defined as

$$S_v(\mathbf{t}) = \frac{\text{total crack length at time } \mathbf{t}}{\text{Area}} \tag{23}$$

After obtaining $S_v(\mathbf{t})$, $\dot{S}_v(t)$ can be calculated by numerical differentiation without any difficulty. Fig. 6 (left) shows the evolution of $S_v(\mathbf{t})$ and $\dot{S}_v(t)$ from the initial time, when the specimen starts loading, up to 500 nanoseconds.
Moreover, the angular crack density distribution $S_v(\theta,\mathbf{t})$ can be calculated, and the rosette shown in the same figure can be constructed. Each point x, y in this rosette is defined as

$$x = S_v(\theta \pm \Delta\theta) \cdot \cos(\theta) \tag{24}$$

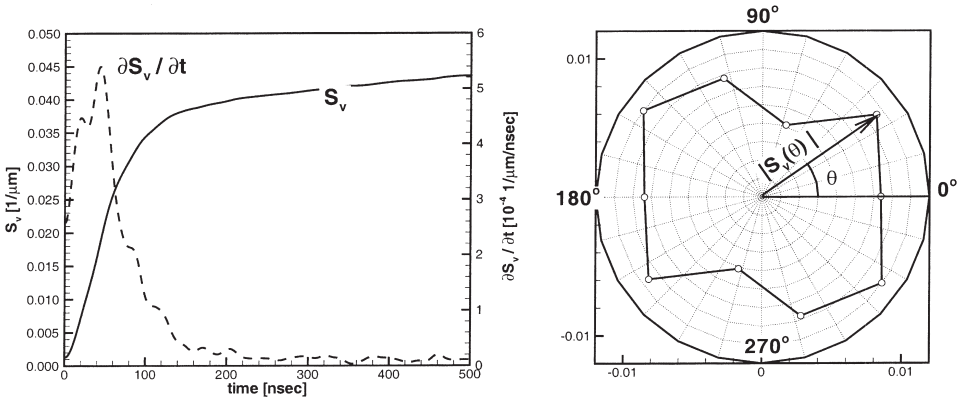

Fig. 6. $S_v(t)$, $\dot{S}_v(T)$ (left) and $S_v(\theta,t_f)$ (rosette, right) for a microstructure of area A=540×190.3 μm^2.

$$y=S_v(\theta\pm\Delta\theta)\cdot\sin(\theta) \tag{25}$$

In other words, the distance from each point to the origin is the crack density for all the cracks with an angular orientation, θ, such that $\theta-\Delta\theta\leq\theta<\theta+\Delta\theta$. The degree of discretization is defined as $\Delta\theta=2\pi/N$, where N is the number of intervals for θ. For example, Fig. 6 (right) is the rosette constructed with a discretization N=10. The reason why a very low discretization factor has been chosen is the small number of potential angles where the crack can occur in our microstructure. Even though these figures show the variation of θ from 0 to 2π, the angle is computed from 0 to π, and the density $S_v(\theta+\pi)$ is assumed equal to the density $S_v(\theta)$. The relationship between $S_v(t)$ and $S_v(\theta,t)$ is: $S_v(t)=\int^{\pi}_{0}S_v(\theta,t)\,d\theta$.

As described earlier and observed in experiments, ceramics are so susceptible to fragmentation that they can pulverize upon unloading if enough damage and elastic energy is stored within the material in the loading phase. This makes the recovery of samples very difficult in experiments. The possibility of material pulverization in unloading is investigated with the microstructural model.

Unloading is simulated by removing the traction boundary conditions on the top and bottom surface of the specimen at time t=500 nsec. The condition of uniform **u**, **v** and **a** at the top and bottom nodes of the specimen is also removed while the periodic boundary conditions, at, x=0 and x=L are retained after unloading. Fig. 5 shows the evolution of fragmentation upon unloading. It is observed that crack coalesence occurs leading to the formation of fine fragments. If the periodicity of the RVE is taken into account, a clear picture of material pulverization is inferred from these calculations. The final fragment size correlates with the interface properties as it will be shown later.

4.2. Effect of representative volume element (RVE) size

As discussed in Section 3.1, the representative volume element is selected such that its height is equal to the thickness of the ceramic specimen, 540 μm (See Fig.

4). However, nothing has been said about the width of the RVE. In order to study the effect of varying this width, a real microstructure is digitized and the finite element mesh is generated for each one of the grains, then four different RVEs are taken from the original RVE keeping the same shape and size of the grains, but varying the original width (190.3 μm as given in the original photography) by a factor of 1/2, 3/4, 3/2 and 2.

In the same analysis, we have included an RVE of the same size and number of grains as the original, except for the fact that the shape of the grains is different.

Fig. 7 shows the crack area, per unit volume S_v (or crack length per unit area, for 2-D analysis) as a function of time for each one of these microstructures. Even though the response seems to vary with the RVE width, there is no clear trend as

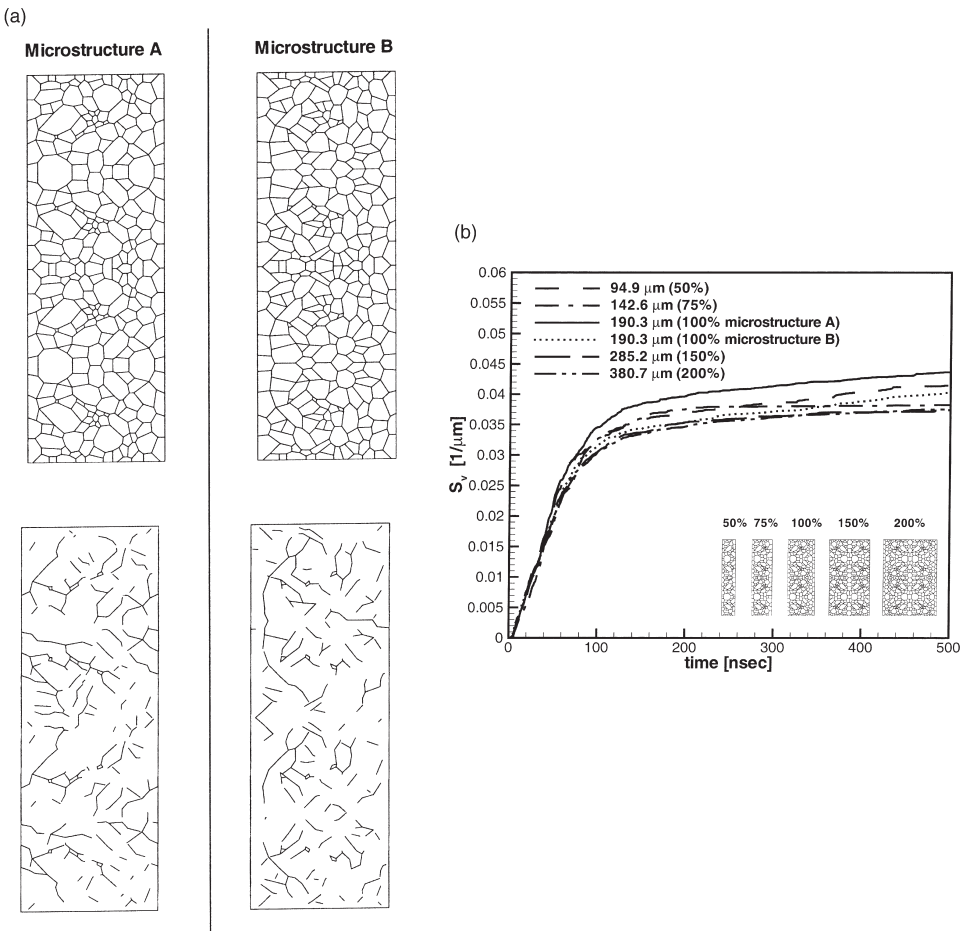

Fig. 7. Effect, of the RVE size: (a) Original microstructure and crack pattern for microstructure (A) and microstructure (B) which have the same original width (b) $S_v(t)$ for each RVE including the original microstructure (A) and microstructure (B).

the width is increased. A maximum variation of about 15% is observed in the maximum value of S_v. In fact, the variation can be considered to be caused by small changes of the grain shape, made "ad-hoc", to preserve the grain periodicity at the boundaries.

The variation of S_v for the case with 100% of the original RVE but different grain shape is included in the same figure, showing a variation of the same order as the one resulting from variations in the RVE width. These results need to be interpreted with caution in view that larger variations may result, for other parameters of the cohesive law.

The crack patterns of the two microstructures with the original RVE size are also shown in Fig. 7. The crack pattern for the microstructures with different RVE width can be seen in Fig. 8. The visual effect in this case is stronger than the evolution of crack density where a similarity in crack patterns can be readily appreciated.

Subsequent analyses included in this paper will be presented using the original microstructure, unless otherwise specified.

4.3. Effect of T_{max} and K_{IC}

A parametric study of the variation of the two main interface parameters, K_{IC} and T_{max}, is carried out. These parameters are the material toughness of the ceramic, K_{IC}, and the maximum interface strength, T_{max} utilized in Eqs. (7)–(11).

Six cases were studied for two different values of K_{IC} (1.7 and 4 MPa·m$^{1/2}$) and three different values of T_{max} (1, 5 and 10 GPa) combined as it is shown in Table 3. In all these cases $\delta=\delta_n=\delta_t$, and $\alpha=1$.

Fig. 9 shows the crack pattern for each one of these six cases. In these sequences the different extent of crack nucleation and crack propagation can be appreciated. For the case with K_{IC}=1.7 MPa·m$^{1/2}$ and T_{max}=1 GPa, most interface elements are

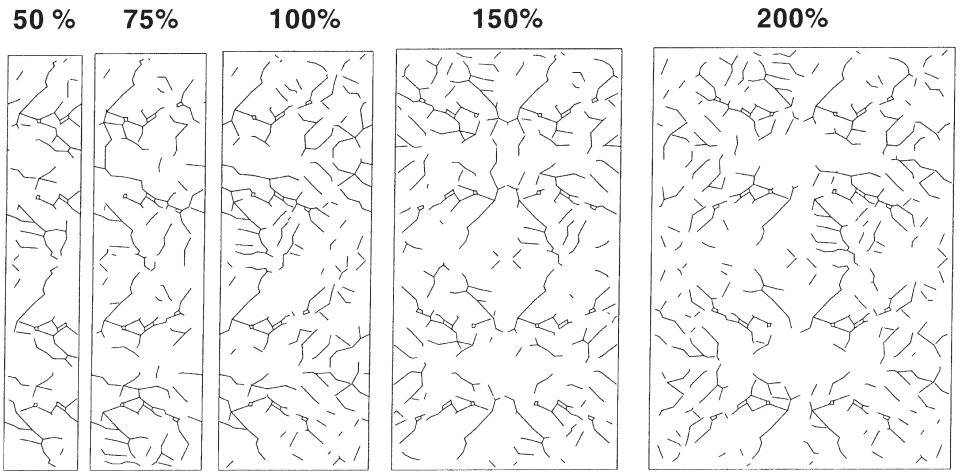

Fig. 8. Crack pattern for microstructures with different RVE sizes.

Table 3
Interface parameters used for the study of the effect of T_{max} and K_{IC}

K_{IC} ($MPa{\cdot}m^{1/2}$)	G_I (N/m)	δ (μm) for T_{max}=1 GPa	δ (μm) for T_{max}=5 GPa	δ (μm) for T_{max}=10 GPa
1.7	7.092	0.01418	0.002837	0.001418
4	39.26	0.07853	0.015706	0.007853

broken as the wave advances. On the contrary, with the same K_{IC} and T_{max}=10 GPa, a dilute distribution of cracks is achieved. It should be pointed out that 10 GPa represents a cohesive strength close to the theoretical value $E/20$. In other words, grain boundaries without impurities and good lattice matching.

The case with K_{IC}=4 MPa·m$^{1/2}$ and T_{max}=1 GPa presents a different crack pattern as all the other cases. The cases with K_{IC}=4 MPa·m$^{1/2}$ and higher values of the maximum strength, T_{max} experience interface element breakage only in the corner of the voids, showing the effect of stress concentration and void collapse.

Fig. 10 shows the crack length per unit area, $S_v(t)$, as a function of time for each one of these six cases. The rosette $S_v(\theta,t_f)$ for t_f=500 nsec is also shown in the same figure. The evolution of the crack density is more evident for the cases with weak interfaces.

Fig. 11 shows the pulverization pattern for each one of these cases at 400 nanoseconds after the unloading. As mentioned before, these ceramics are so susceptible to fragmentation that they represent the most difficult problems in wave propagation investigation with specimen recovery. These calculations demonstrated that the pressure–shear configuration presented by Espinosa et al. (2000a), would be more attractive for investigating other materials, with higher toughness, in which damage, plasticity, or phase transformation induced by lateral wave release are minimized.

The velocity profiles at the bottom face of the specimen have also been analyzed. Fig. 12(a) shows the normal velocity for all the six cases. The three curves on the left correspond to the runs with K_{IC}=1.7 MPa·m$^{1/2}$ and the ones on the right correspond to the runs with K_{IC}=4 MPa·m$^{1/2}$. An initial jump in normal velocity, followed by the reverberation of waves within the specimen is observed. It can be appreciated that the particle velocity rate changes as T_{max} is varied. The higher the value of T_{max}, the higher the velocity rate up to a steady state at a maximum normal velocity of about 70 m/s. The cases with K_{IC}=4 MPa·m$^{1/2}$ and T_{max}=5 GPa and 10 GPa have similar velocity histories. The same effect is observed in the transverse velocity (Fig. 12(b)). The elastic prediction of the normal and transverse velocities, which are included in the figures, are given by

$$v_1(x,0,500\text{nsec})=\frac{2(\rho c_s)_s(\rho c_s)_f}{[(\rho c_s)_s+(\rho c_s)_f]^2}V_0\sin\gamma \tag{26}$$

$$v_2(x,0,500\text{nsec})=\frac{2(\rho c_l)_s(\rho c_l)_f}{[(\rho c_l)_s+(\rho c_l)_f]^2}V_0\cos\gamma \tag{27}$$

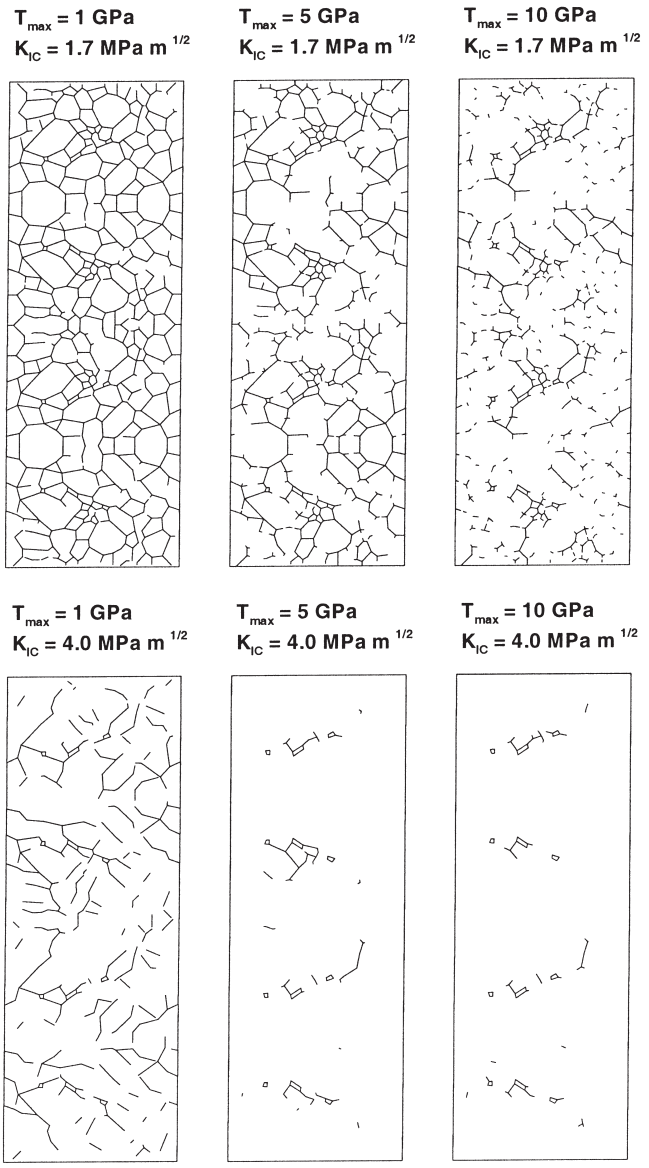

Fig. 9. Crack pattern for different values of material toughness and interfacial strength at 100 nanoseconds.

Average material moduli are used in these elastic predictions.

The transverse velocity has a rising slope that, is clearly dependent on T_{max}. This is clue to the rate of damage as inferred from the S_v plots. Despite the fact that significant microcracking occurs for the case K_{IC}=1.7 MPa$\sqrt{m}$ and T_{max}=1 GPa, it is

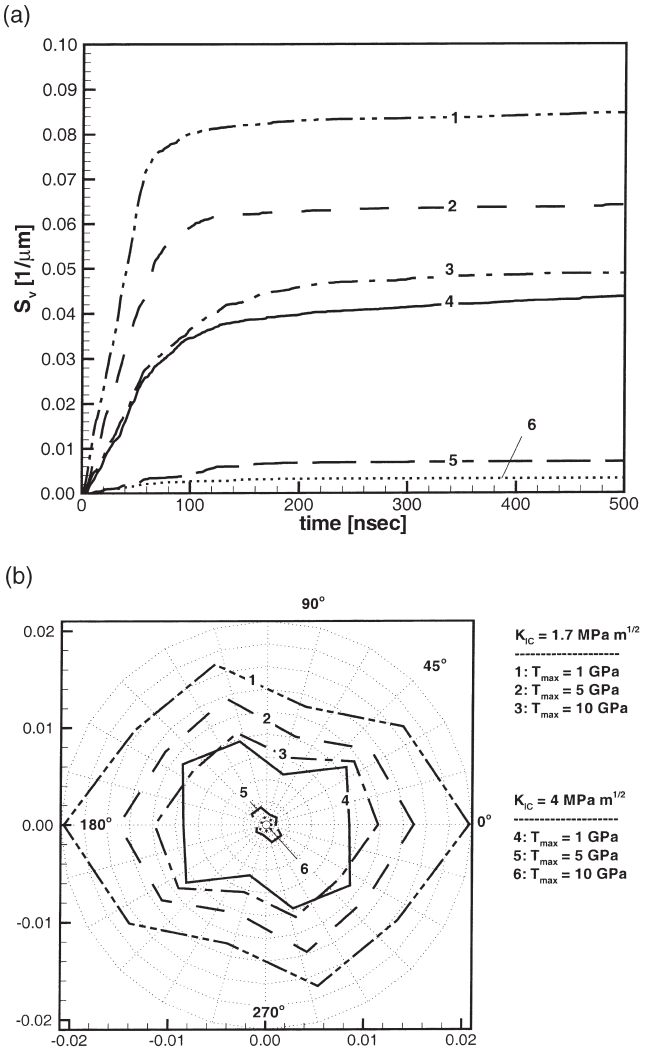

Fig. 10. $S_v(t)$ (left) and $S_v(\theta,t_f)$ (rosette, right) for different values of material toughness and interfacial strength.

seen that the maximum transverse velocity reaches and exceeds the elastic prediction. This feature is in contrast with the experimentally measured transverse velocity history (Espinosa et al., 2000b), in which the free surface transverse velocity is about half the elastic prediction and decays progressively after the attainment of a peak value. Two effects can contribute to the experimentally observed decay in transverse velocity: they are: i) the possibility of sliding at the flyer–specimen and specimen–target interfaces, ii) transgranular cracking leading to a favorable crack pattern. None

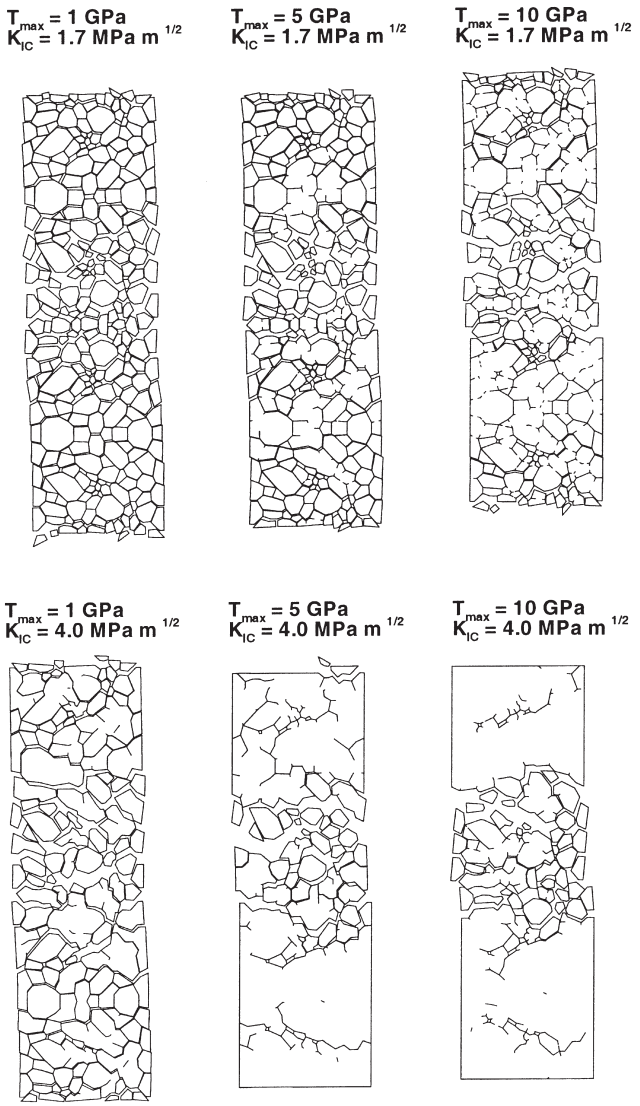

Fig. 11. Pulverization pattern for different values of K_{IC} and T_{max}.

of these features were accounted for in the present simulations. Because of their complexity, they will be addressed in future work.

Another feature to be noted is the fact that both the maximum transverse and normal velocities exceed the elastic prediction. This can be explained by the assumption of a 2-D microstructure and therefore not a fully random microstructure. The latest is assumed in the calculation of polycrystalline average moduli which were used in the calculation of elastic wave velocities.

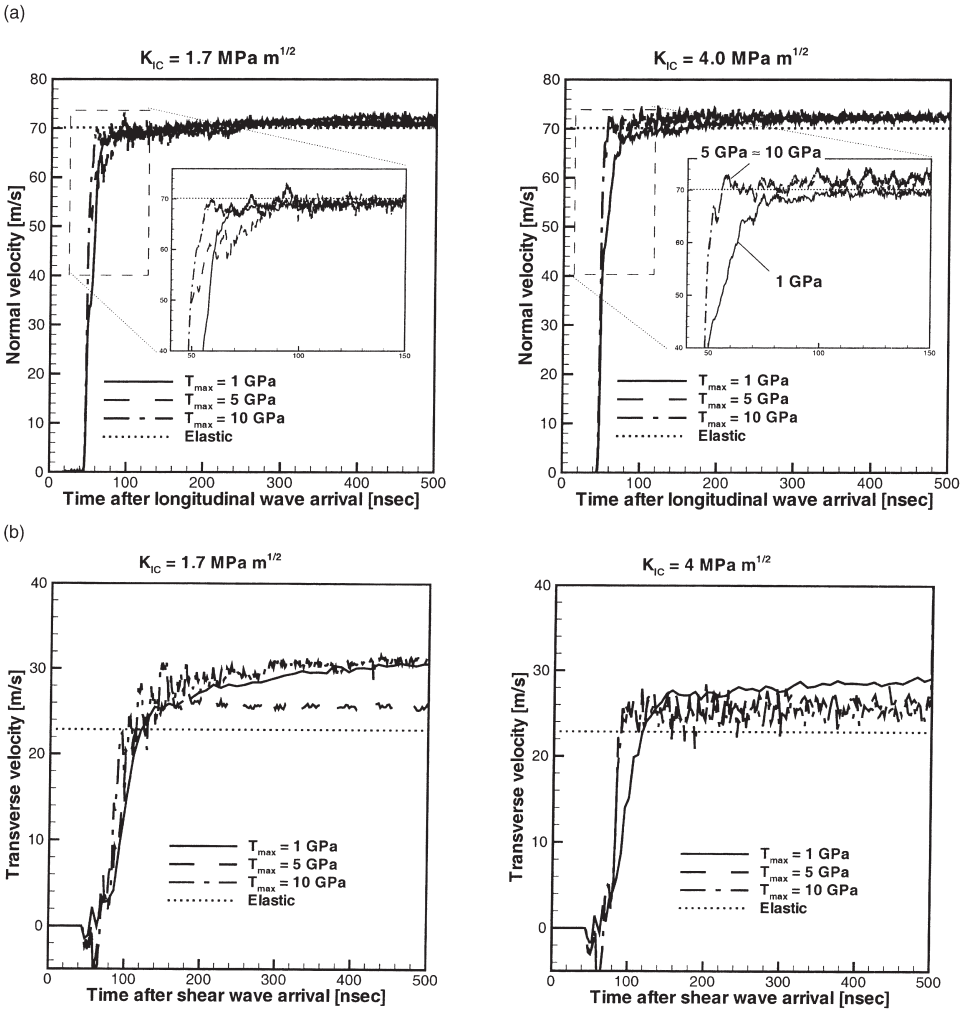

Fig. 12. (a) Normal velocity history for different values of K_{IC} and T_{max} (b) Transverse velocity history for different values of K_{IC} and T_{max}.

4.4. Effect of initial defects

As observed in Fig. 9, the case with the strongest interface K_{IC}=4 MPa·m$^{1/2}$ and T_{max}=5 GPa shows a very small crack density compared with the cases with weaker interfaces. In this case, the microcracks could only nucleate on the voids and propagate into the microstructure. Hence, this case is very suitable for studying the effect of initial defects. Physically, initial defects are generated during material sintering because of elastic and thermal grain anisotropy, see Tvergaard and Hutchinson (1988).

A new simulation has been carried out where a uniform distribution of initial

defects has been included with size ≈1 μm located at triple points. Fig. 13 shows the crack length per unit area, comparing the same case with and without initial defects. The initial crack length per unit area for the first case, which was not included in the evolution of $S_v(t)$, is $S_v(0)$=0.005452/μm. The crack patterns at time 0 and 500 nsec are shown in the same figure. This demonstrates the fact that a microstructure with an initial distribution of flaws, which can be a more realistic case to analyze, is more susceptible to microfracture than an "*ideal*" microstructure without any defects.

4.5. Effect of grain elastic anisotropy

Several investigations have been reported about the effect of crystal anisotropy on polycrystalline materials response.

Ortiz and Suresh (1993) studied the residual stress generated in polycrystalline ceramics, during cooling from the fabrication temperature, finding that the stress distribution is affected by elastic anisotropy.

Mullen et al. (1997) developed a finite element-based Monte Carlo which can be used to predict scatter in the nominal elastic constants of thin films. These moduli have been found to be strongly dependent on the anisotropy level of the material.

Tvergaard and Hutchinson (1988) analyzed the effect of crystal anisotropy on the formation of grain boundary microcracks by considering a planar array of hexagonal grains as a model of polycrystalline ceramics. Stress singularities at triple points and

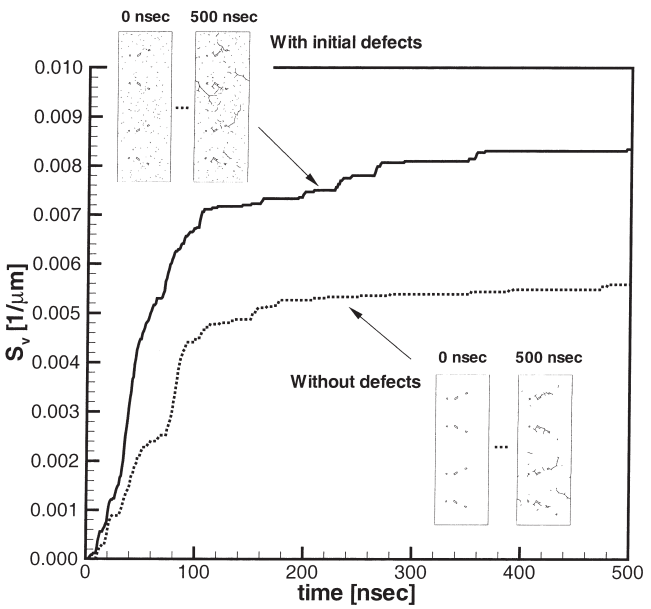

Fig. 13. Crack length per unit area and crack patterns for a microstructure with strong interfaces, with and without initial defects.

grain-boundary defects were also examined. The stress at those points can increase according to the grain elastic anisotropy, which results in a smaller critical grain size for microcracking.

Grah et al. (1996) conducted computer simulations in polycrystalline specimen using a spring-network model for arbitrary in-plane crystal anisotropy. From those simulations, intergranular crack paths were obtained.

In this section the stochastic effect of grain elastic: anisotropy and its impact on the fracture behavior of the ceramic at the microlevel is studied.

Four identical microstructures are considered for this analysis. The only difference between them is that the principal material directions are generated randomly in three of them, while only isotropic elasticity, average values for the polycrystalline material, is considered for the fourth case.

This parametric study allows us to see if the fact that each grain has random principal material directions presents significant variations in the RVE response. Also, it addresses the question of what is the effect of this misorientation on intergranular crack growth regardless of the interfacial strength.

The crack length per unit area $S_v(t)$, for four cases, is shown in Fig. 14. A clear tendency of higher values of S_v, for the anisotropic cases can be appreciated. Even if the crack patterns look very similar, this is a case where a stereological study is more useful to *highlight* the real differences. Not only variations in maximum S_v at 500 nsec are observed, but also a higher rate of crack growth, in the first 100 nsec, is manifested in the case of RVEs with elastic anisotropic grains.

Fig. 15 provides even more information on microcrack evolution. At triple points, the stress concentration effect is more important where the grains are described by

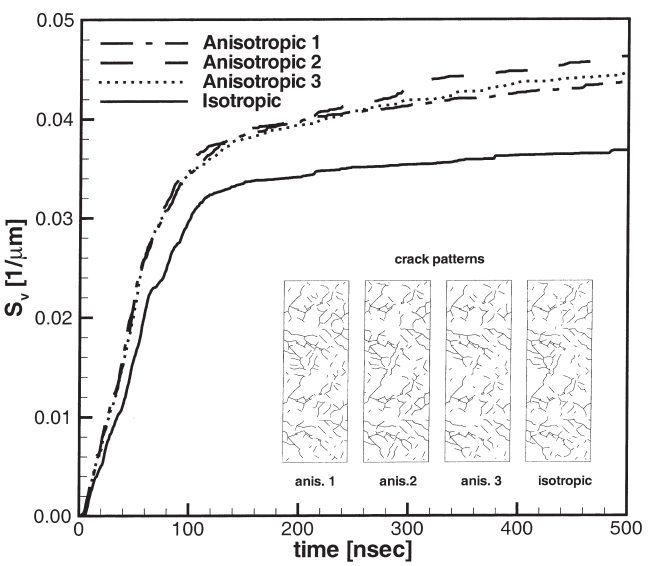

Fig. 14. Effect of grain anisotropy in the crack area per unit volume. Higher stress concentrations at triple points are observed in the case of RVES with elastic anisotropy.

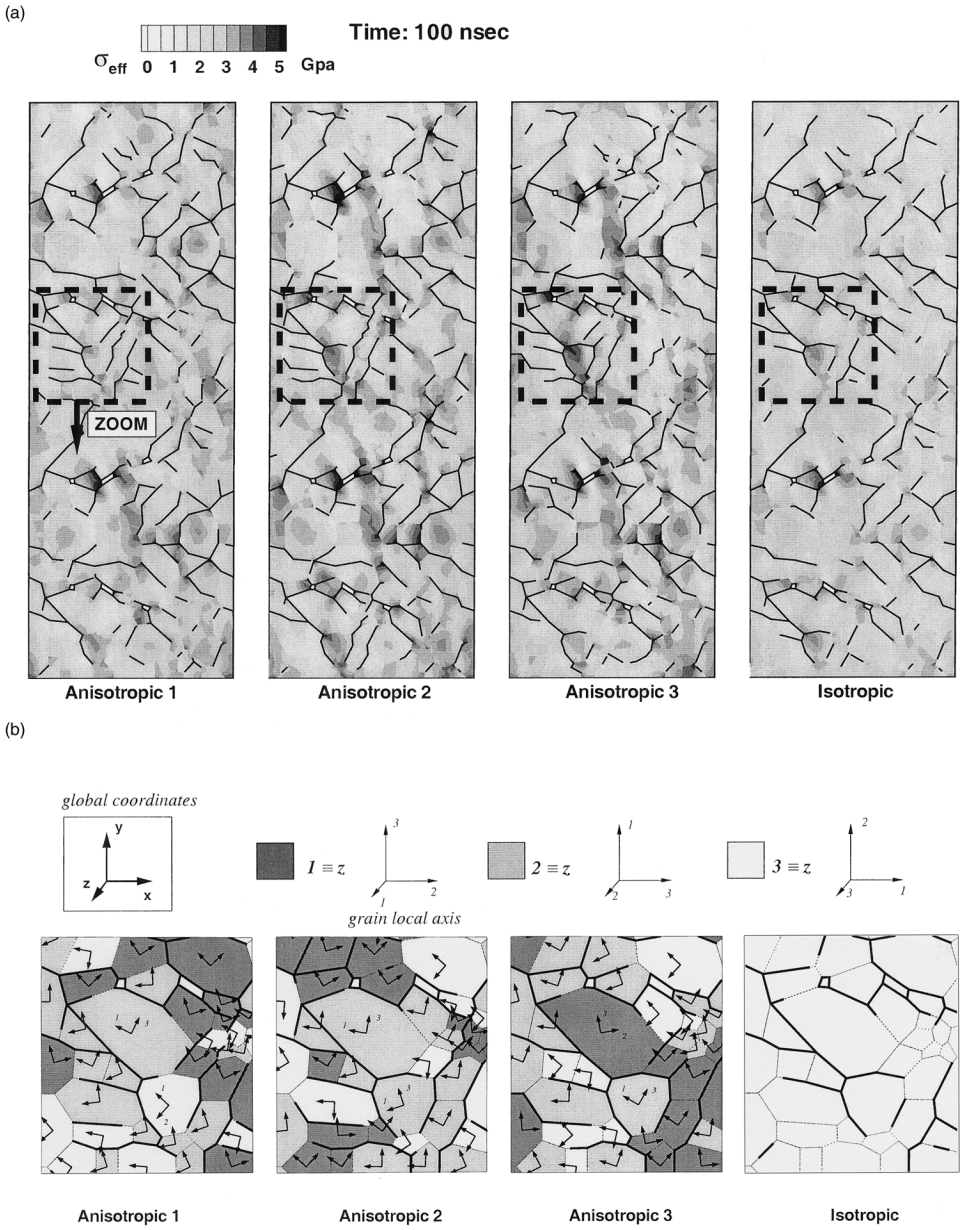

Fig. 15. Effect of grain anisotropy: (a) Crack pattern showing the distribution of the effective Cauchy stress σ_{eff} for the three cases with grain elastic anisotropy and the case with elastic isotropy. (b) Zoom showing crack pattern and grain orientations.

different principal material directions. For the isotropic case, the stress concentration effect is minimum. Future studies will focus on the effect of residual stresses, introduced during cooling from the sintering temperature, in the mechanical response of ceramics.

4.5.1. Effect of considering the ceramic to be transversely isotropic

As it was mentioned in a previous section, alumina is known to be a trigonal atomic system making the assumption of plane strain inappropriate if the local axes 2 or 3 coincide with the global axis z. This implies only two choices: 1) considering only the case where $1 \equiv z$ similar as what was considered in Ortiz and Suresh (1993) and Tvergaard and Hutchinson (1988); 2) approximate the ceramic to be transversely isotropic, $C_{14}=0$, and all three cases $1 \equiv z$, $2 \equiv z$, $3 \equiv z$, randomly chosen, as it is considered in this paper. Fig. 16 shows the comparison of the crack density between the case considering $C_{14}=0$ using the three planes of symmetry and the case with $C_{14}=101$ GPa (Hearmon, 1956) but using only $1 \equiv z$. The isotropic case has been

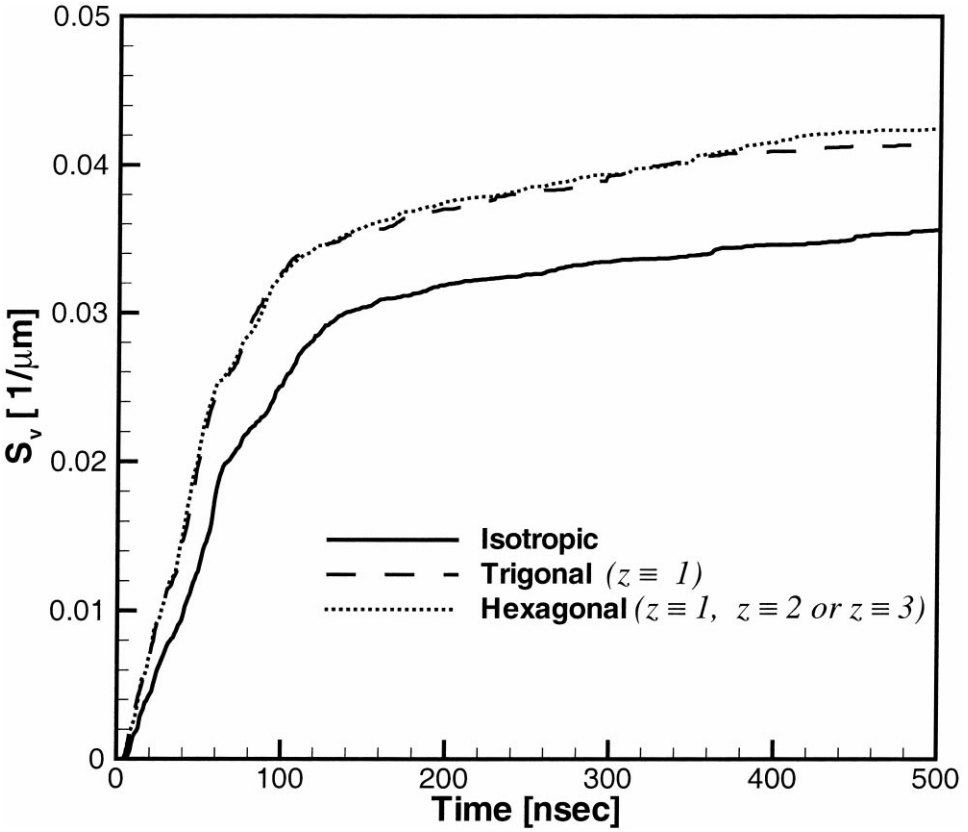

Fig. 16. Effect of considering the ceramic as an orthotropic system instead of trigonal in the evolution of the crack density.

also included in the figure for comparison purposes. The simulations show that both anisotropic cases lead to similar values of S_v and $\dot{S}_v$.

4.6. Effect of grain size

In addition, an analysis comparing a microstructure with smaller grain size has been carried out. In all the previous simulations the averaged grain size of the microstructure was 22 μm. A second microstructure, with an average grain size of 11 μm, was used in simulations under the same conditions in order to study the evolution of crack density. Due to the significant number of grains and the CPU time that the multi-body contact algorithm consumes, the analysis has been carried out only up to 150 nanoseconds.

Fig. 17(a) shows the crack length per unit area, for both cases. It can be observed that the curve showing the evolution of S_v is significantly lower for the case with smaller grains. These results are consistent with the findings of Ortiz and Suresh (1993), where numerical simulations of intergranular fracture during cooling from the fabrication temperature have been carried out using an interface cohesive model. A similar behavior was also observed experimentally on creep deformation of alumina–silicon carbide composite by Lin et al. (1996). Fig. 17(b) shows the original microstructure together with the crack pattern at 150 nanoseconds.

A more extensive analysis needs to be done in order to study the behavior of ceramics with different grain sizes and examine its effects under different loading conditions. The aim of the study presented in this paper is to provide a tool that allows those kinds of investigations. Future work will address the modeling of microstructures with large distributions of grain sizes and shapes including texture.

4.7. Effect of stochastic distribution of interface properties

The interfaces between different material phases are important in determining many bulk properties. One of the simplest interface types is the boundary between two crystals of the same material. If two crystals of exactly the same orientation are brought together, they fit perfectly. However, if the crystals are slightly tilted and brought back together, there is a disregistry at the interface, which is equivalent to insertion of a row of dislocations. The number of dislocations per unit length and the energy of the boundary increase as the angle of tilt increases. If instead of being tilted, the two grains are rotated, the result is a grid of screw locations that are more complex to represent diagrammatically but are basically similar to the tilt boundary. A combined tilt and rotation corresponds to a complex combination of edge and screw dislocations. There is a well-known model that characterizes the structural order at grain boundaries through a parameter that measures the reciprocal density of coincident lattice sites (Σ), the so-called coincident-site lattice model (CSL) (Bollmann, 1970). Low values of Σ correspond to a high density of coincident lattice sites. Atomistic computations, (Tasker and Duffy, 1983; Wolf, 1984), reveal that special low energy interfaces are found for $\Sigma<29$. It was observed that there is a tendency for boundaries with $\Sigma<29$ to be resistant, to cracking and those with $\Sigma>29$

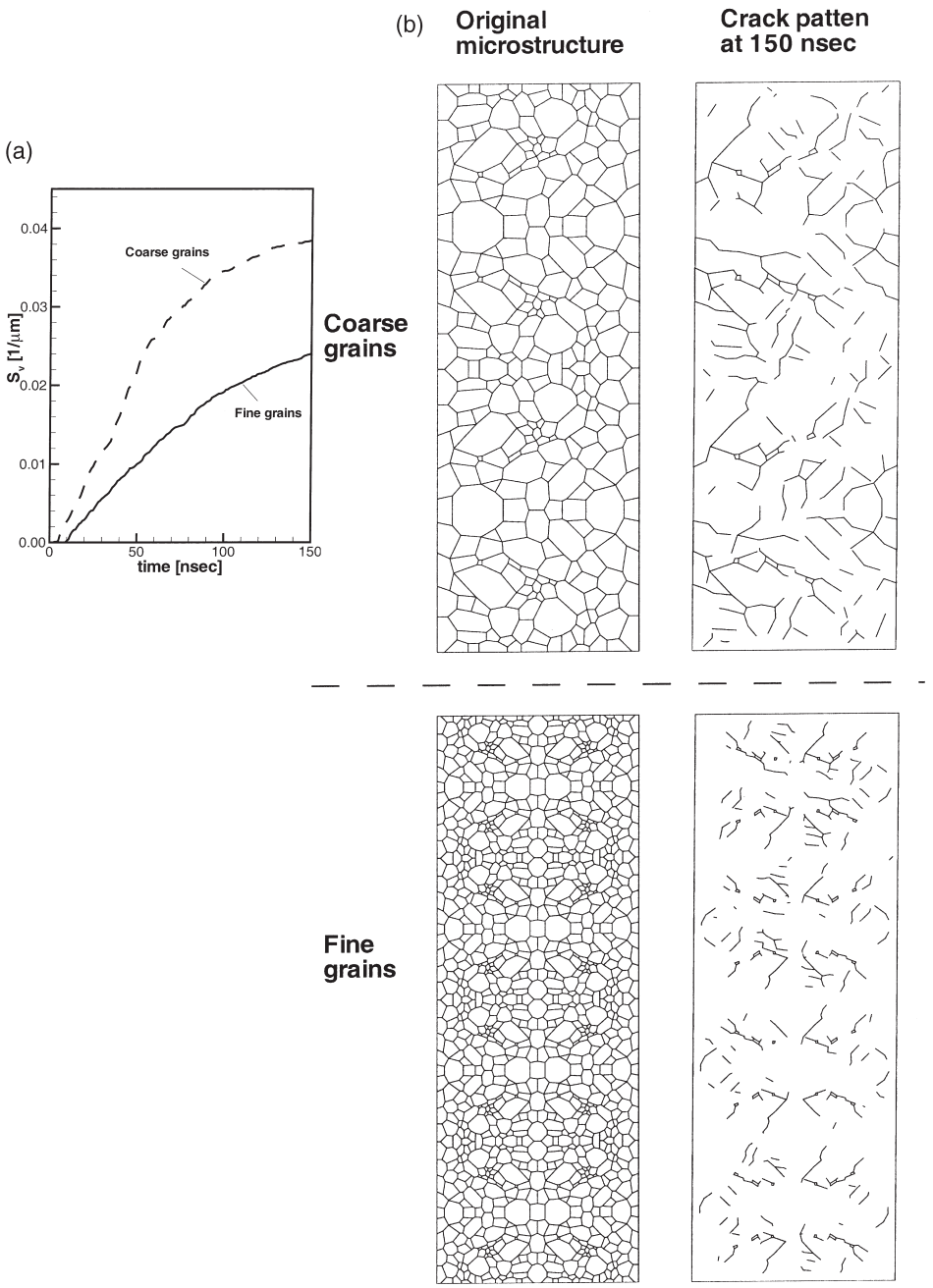

Fig. 17. Effect of grain size. (a) Crack length per unit area for the cases with coarse and fine grains. (b) Original microstructure and crack patterns at 500 nsec.

to be susceptible to cracking. Boundaries with $\Sigma>29$ are referred to as random boundaries. Fig. 18(a) shows a high resolution transmission electron microscope (HRTEM) picture of a high-angle alumina–alumina interface (Espinosa, 1992).

Several investigators have studied the interfacial properties of Al_2O_3/SiC by transmission electron microscopy (TEM), (Jiao et al., 1997; Luo and Stevens, 1997; Sternitzke, 1997). They have found that the magnitude of the interfacial fracture energy between SiC and alumina is over twice the grain boundary fracture energy, and grain boundaries are strengthened by SiC nanoparticles due to the stronger interfaces.

Not only the grain misorientation affects the interfacial strength, but also the presence of glassy phase and glass pockets is an important factor to be taken into account (Simpson and Carter, 1990). Either from impurities present in the powder, sintering aids, and/or contaminants transported through the vapor phase from the hot furnace or container walls to the material being fired, a second phase is sometimes formed at the grain boundaries with an amorphous structure. High resolution electron microscopy micrographs were taken by Espinosa (1992), at the interfaces of a glass pocket (see Fig. 18(b)).

The random distribution of glass pockets, glassy phases, SiC nanoparticles, defects and other impurities leads to the consideration of a statistical variation in the interfacial strength dependent on the grain misorientation. Data on grain boundary toughness as a function of coincident lattice sites are very limited and incomplete in the literature. For this reason, the stochasticity of the microfracture process with distributions which are independent of the principal material directions, has been analyzed.

4.7.1. Weibull distribution of interface parameters

If a large number of identical samples were to be tested and the strength distribution of a brittle and a ductile solid plotted, they would look different. The strength distribution curve for ductile solids is very narrow and close to a *Gaussian* or *normal distribution*, while that for brittle solids is very broad with a large tail on the hit-strength side that can be explained by a statistical distribution called the *Weibull distribution*, named after the Swedish engineer who first proposed it (Weibull and Sweden, 1951).

In this analysis, the interfacial strength parameters will be described by a *Weibull* distribution. Since only two interface parameters can be varied, two distributions will be considered: varying K_{IC} and keeping T_{max} constant, and vice versa.

The Weibull distribution for K_{IC} and T_{max} are:

$$f(K_{IC})=\frac{m(K_{IC})^{m-1}}{K_{IC}^{0\,m}}\exp\left[-\left(\frac{K_{IC}}{K_{IC}^{0}}\right)^{m}\right],K_{IC}>0 \tag{28}$$

$$f(T_{max})=\frac{m(T_{max})^{m-1}}{T_{max}^{0\,m}}\exp\left[-\left(\frac{T_{max}}{T_{max}^{0}}\right)^{m}\right],T_{max}>0 \tag{29}$$

Where K_{IC}^0 and T_{max}^0 are material constants and m is the *Weibull modulus*, which is a measure of the variability of the strength of the material. Generally, m=5-10 for the case of brittle ceramic samples.

(a)

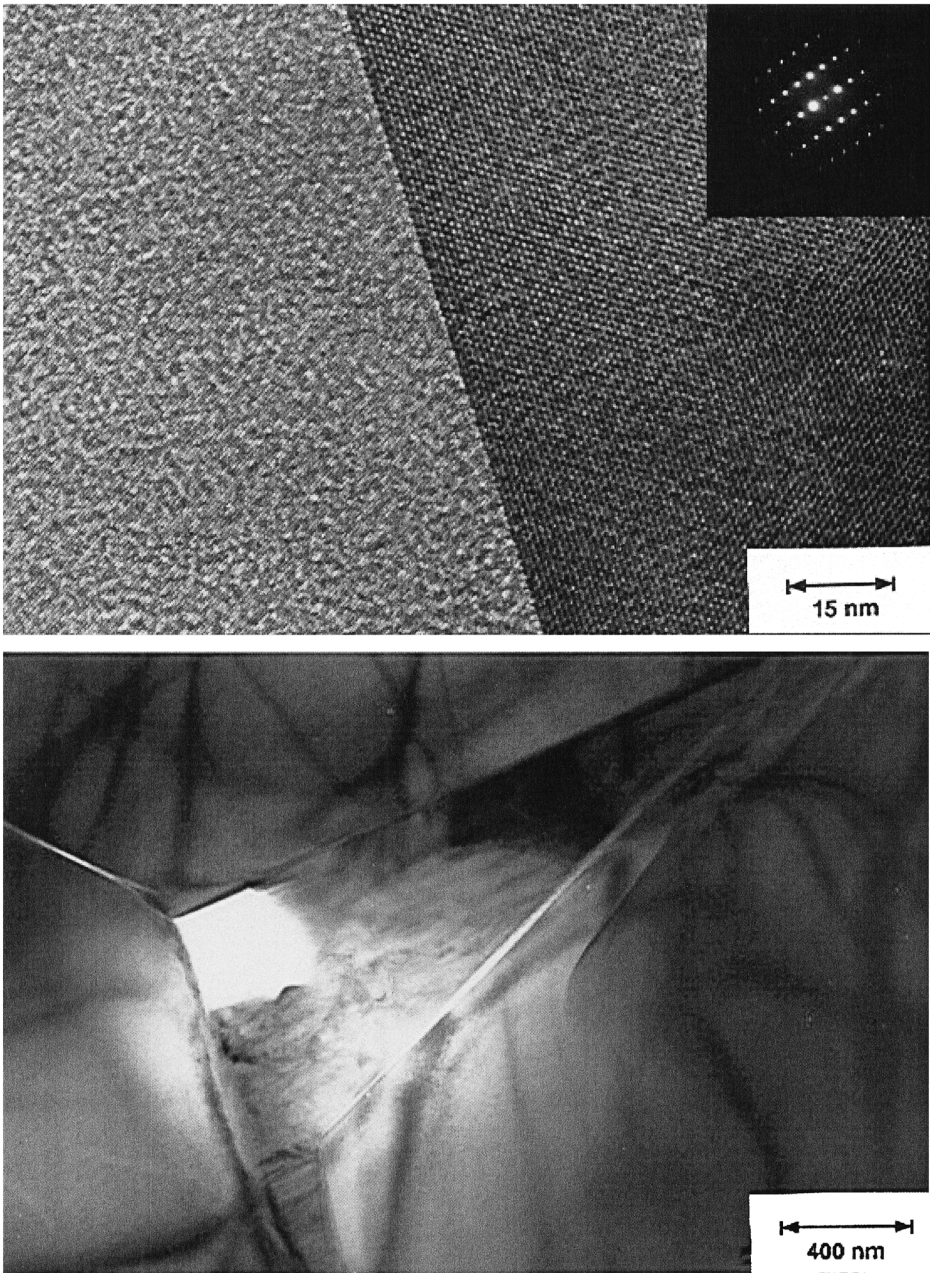

(b)

Fig. 18. (a) HRTEM image of a typical high angle grain boundary. (b) TEM bright field image of a glass pocket, in alumina.

The distribution is such that a grain facet will have the same interface element parameters. In this way there will be only N_f different interface elements (N_f=number of facets in the microstructure).

For the case where K_{IC} varies, the Weibull parameters are K^0_{IC}=4 Mpa·m$^{1/2}$ and T_{max}=1 GPa. Two values of m are taken as m=3.6 (where the Weibull distribution approximates the normal distribution) and m=10. For the other case, K_{IC}=4 MPa·m$^{1/2}$ and T_{max}=1 GPa.

Since the interface parameters are randomly assigned, two simulations with different seeds were carried out for each one of these four distributions. This makes a total of eight simulations. All the simulations are done with the same microstructure having the same principal material direction distribution.

Fig. 19 shows the crack length per unit area, S_v, for each pair of the four different distributions. For comparison purposes, the evolution of S_v for the case with interface with constant K_{IC} and T_{max} is shown in the same curve. The overall response for the cases with the distribution $f(K_{IC})$, given in Eq. (28), seems to be weaker than the cases with distribution $f(T_{max})$. The weakest case presents a 12% increment in the crack density with respect to the case without interface parameter variation, while the strongest case presents a 20% decrement.

The crack pattern for each one of these simulations is shown below the curve S_v vs t. Although there is not much difference between crack patterns, a slight difference in the crack density between the cases with $f(K_{IC})$ and $f(T_{max})$ can be appreciated. A statistical analysis has been done for one of the previous cases. The distribution of Eq. (29) with K_{IC}=4 MPa·m$^{1/2}$, T^0_{max}=1 GPa and m=10 was utilized in order to carry out fifteen simulations with different seeds. Fig. 20(a) shows the crack length per unit area for each one of these simulations, while Fig. 20(b) shows the histograms of $S_v(t)$ for different times. The *mean* value $\overline{S_v(t)}=(\Sigma_n S^i_v)/n$ and the standard deviation $\Delta S_v(t)=\sqrt{\Sigma_n(S^i_v-S_v)/n}$ are also shown in the figure.

4.8. Effect of grain morphology

It is well established that, the grain structure in polycrystalline materials can be simulated by a Voronoi tessellation. For the two-dimensional case, a plane is divided into M grain-like tiles corresponding to M nuclei that may be thought as nuclei of grains. A grain-like tile T_i is defined as follows:

$$T_i=\{x:d(x,P_i)<d(x,P_j) \text{ for all } i\neq j,\} \tag{30}$$

where P_i represents a nucleus and $d(x,P_i)$ denotes the distance between P_i and x. Each tile is named a Voronoi cell and represents an individual grain that is meshed using Delaunay triangulation.

Several investigators have used this technique to represent polycrystalline materials. Ghosh et al. (1997) utilized Voronoi cells to obtain stereologic information for the different morphologies. In this approach each cell is an element in the Voronoi cell finite-element method (VCFEM).

Liu et al. (1998) proposed a method to investigate the damage evolution under uniaxial tension and reversed shear loading conditions, by means of a combined

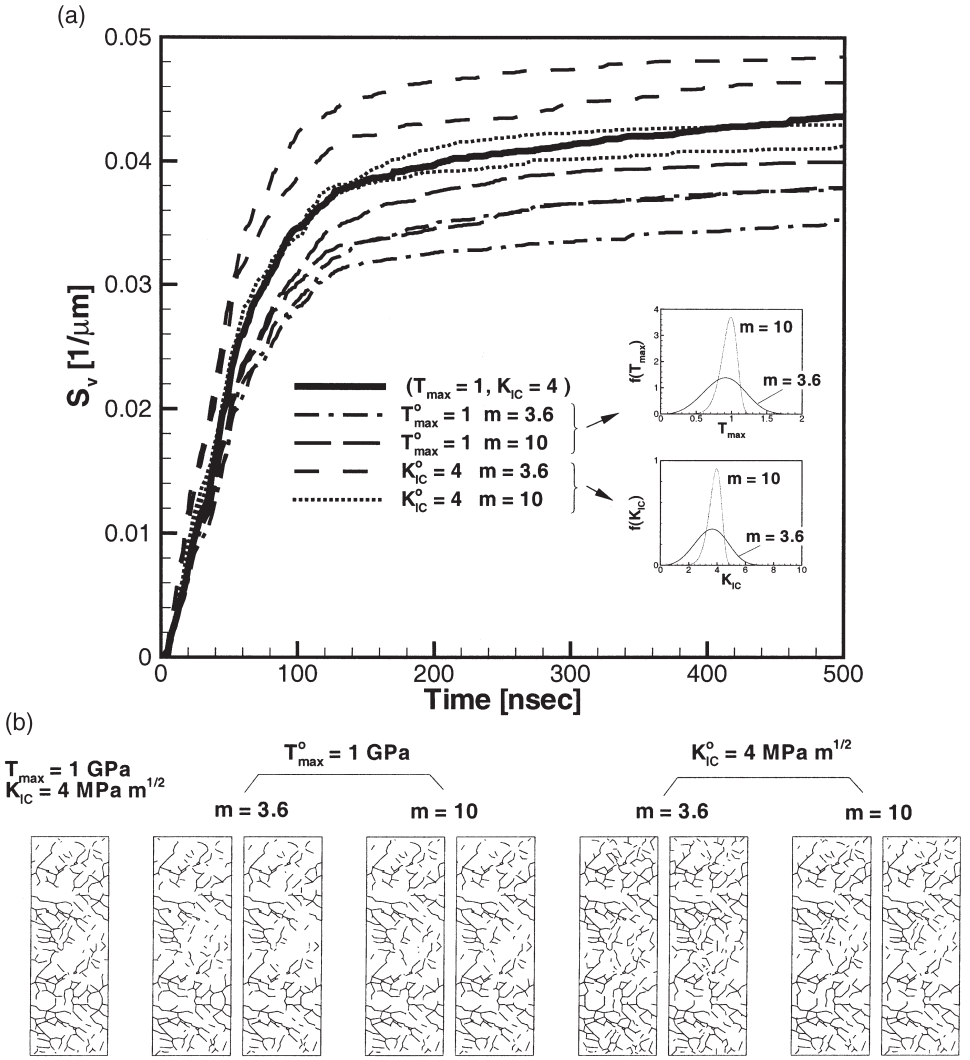

Fig. 19. Effect of the stochastic distribution of interface properties: (a) Crack length per unit area for each distribution. (b) Crack patterns.

continuum damage and mechanism-based cavitation model, using a Voronoi tessellation to represent the polycrystal microstructure.

Bolander and Saito (1998) used Voronoi tessellations to discretize homogeneous, isotropic materials prone to fracture such as cement and concrete. The brittle fracture has been modeled by a rigid-body-spring network.

In order to study the effect of grain morphology, Voronoi tessellations are utilized to generate different randomly shaped microstructures. A cloud of nuclei P_i is randomly generated with a uniform distribution along a specified region of the space

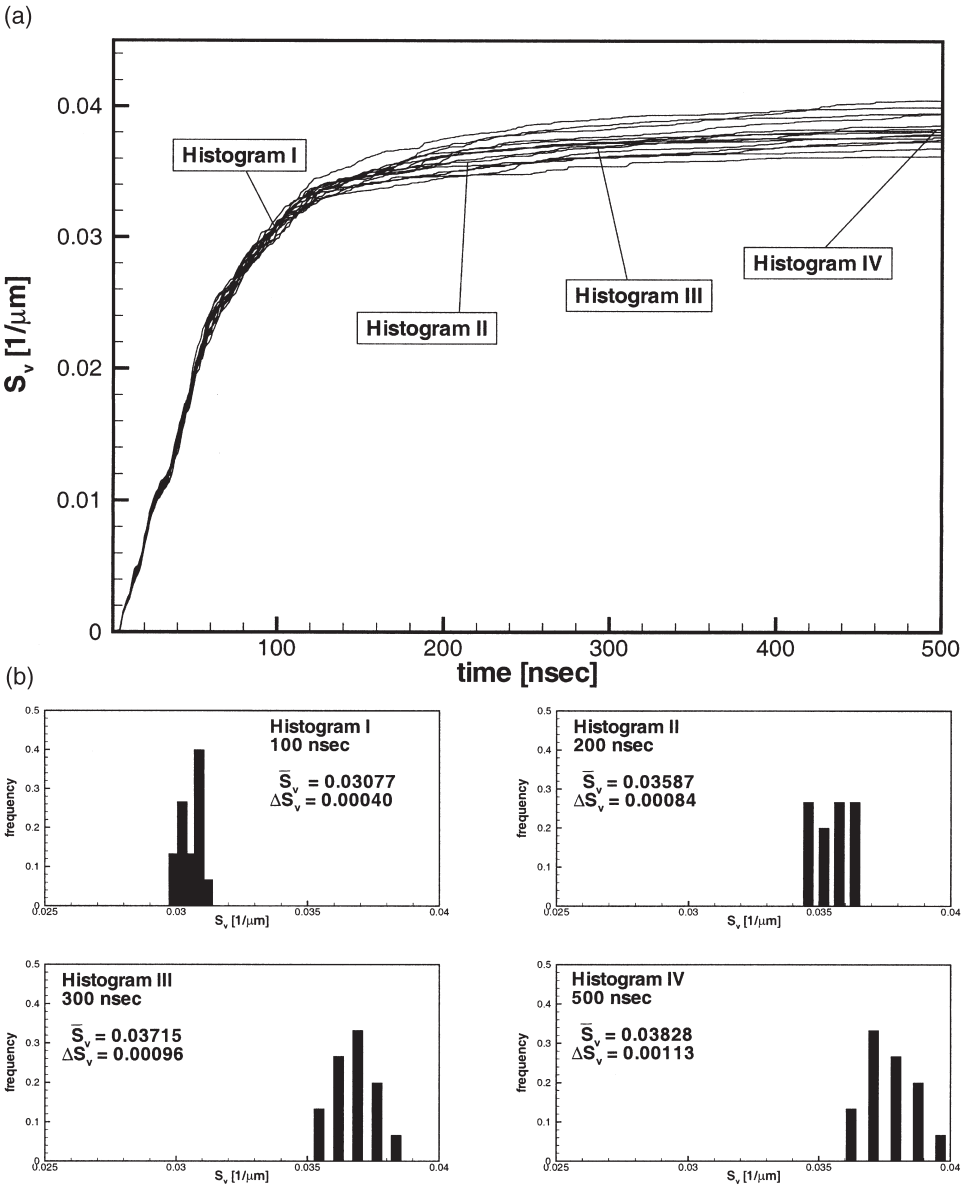

Fig. 20. Effect of the stochastic distribution of interface properties. These are 15 runs with T^o_{max}=1GPa and m=10.

(i.e., microstructure domain). Neighbor nuclei closer than a given tolerance are inhibited in order to limit the minimum grain size. After that, a Delaunay mesh generator is utilized to obtain the Voronoi tessellation associated with the nuclei P_i. We note that the nuclei P_i which are located closer to the borders of the area may

not have sufficient number of neighbors to form a complete polygon. To overcome this difficulty, special care on the microstructure boundary has to be taken.

As it has been explained in Section 2.3, the mesh is generated using triangular elements inside each polygon and four-noded interface elements along the edges, using a multi-body mesh generator. Fig. 21 shows ten microstructures generated using Voronoi tessellations.

These cases were simulated using the same boundary and initial conditions, as well as the material parameters used in the simulations presented in Section 4.1. Fig. 22 shows the crack pattern for each one of the ten Voronoi microstructures at 500 nanoseconds. The crack pattern varies from one microstructure to another and there is no tendency to have the same crack pattern.

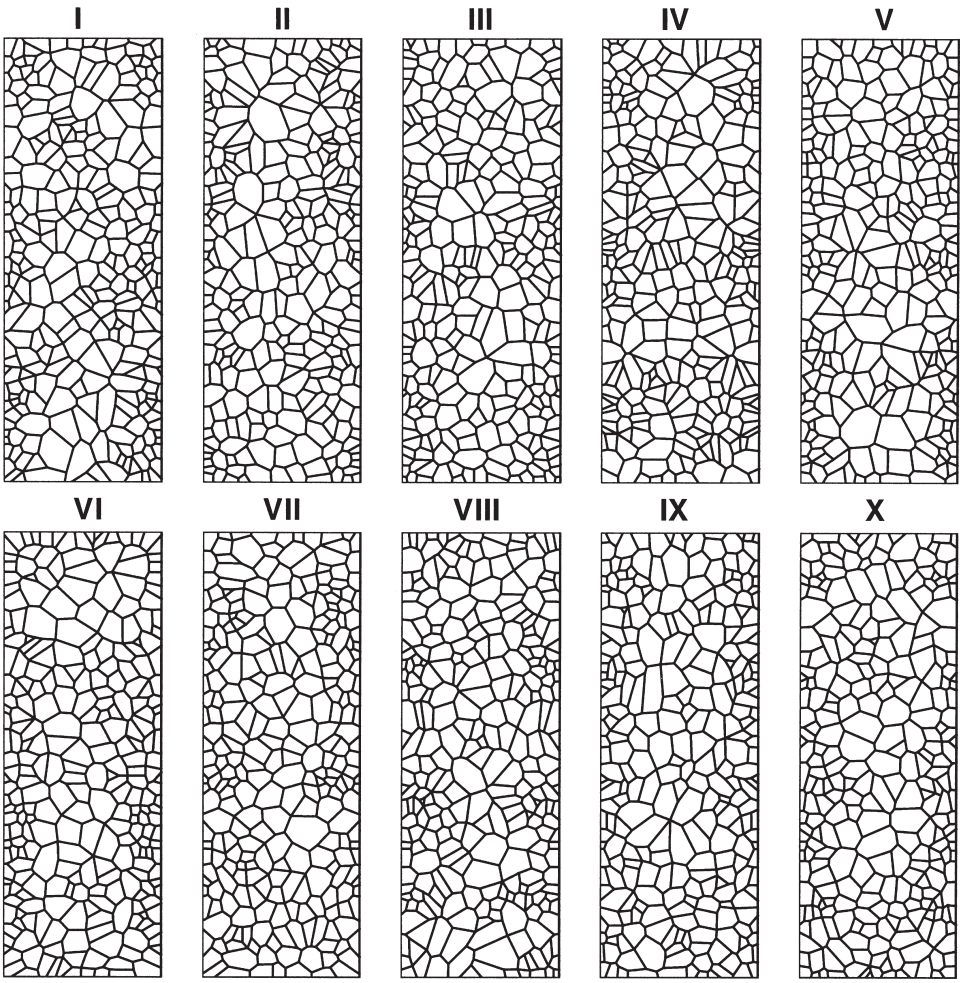

Fig. 21. A total of 10 RVE were generated using Voronoi Tessellation and simulated with our micromechanical model.

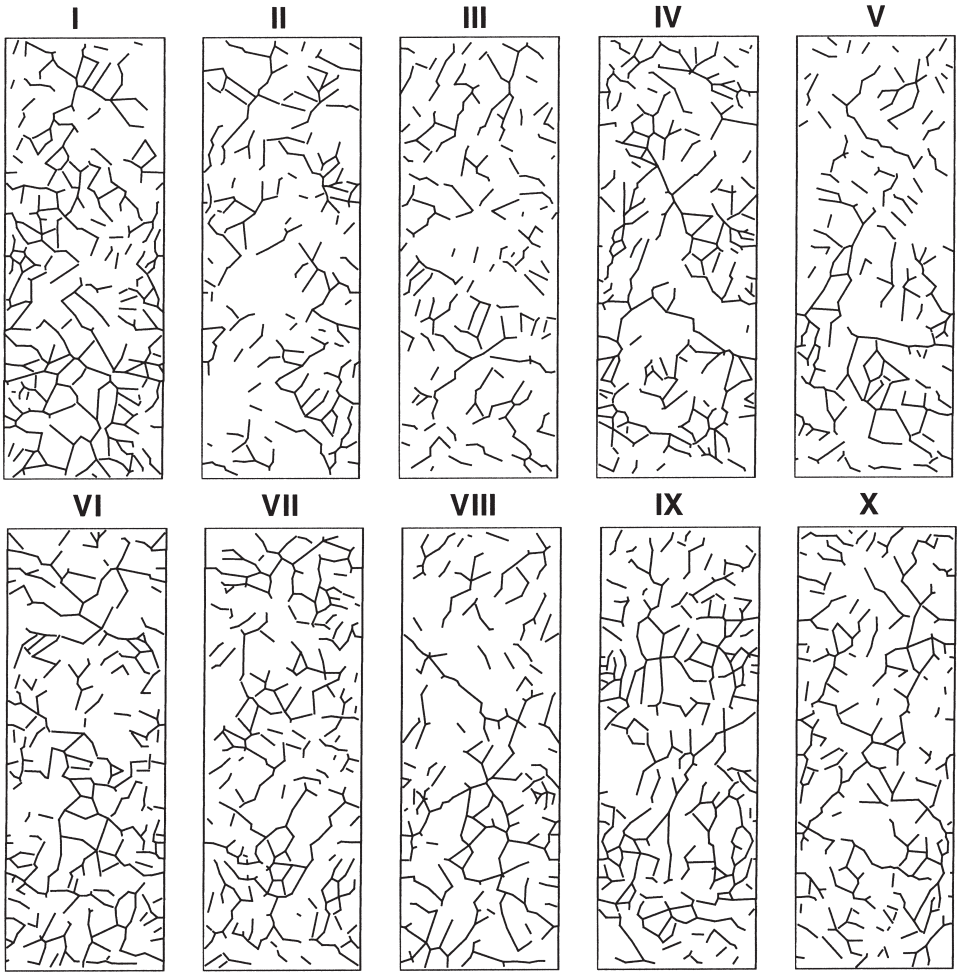

Fig. 22. Microcrack pattern for the 10 randomly generated RVEs.

Fig. 23 shows the crack length per unit area compared with the original case, i.e., digitized microstructure. A histogram of S_v at, 500 nanoseconds is shown in the same figure. The mean $\overline{S_v}$ and the standard deviation ΔS_v are 0.0426/μm and 0.0061/μm, respectively. The effect of the grain shape on the crack density is significant not only for the final crack density but also for its growth rate.

5. Concluding remarks

A model was presented for the dynamic finite element analysis of ceramic microstructures subjected to multi-axial dynamic loading. The model solves an initial-

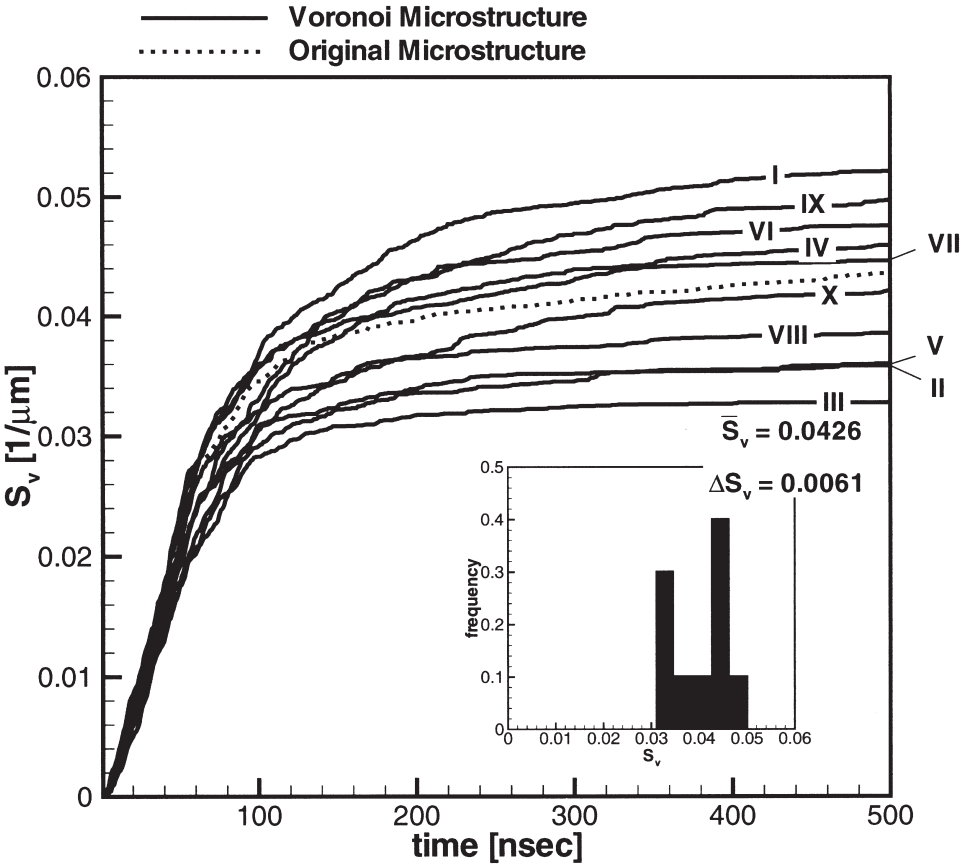

Fig. 23. Crack length per unit area, compared with the original case with the digitized microstructure.

boundary value problem using a multi-body contact model integrated with interface elements. It simulates microcracking at grain boundaries and subsequent large sliding opening and closing of the microcracks. Numerical results are shown in terms of microcrack patterns and evolution of crack density. Simulations with different values of interface parameters show that the crack density is strongly dependent on toughness, K_{IC}, and maximum traction, T_{max}. A parametric study of the representative volume element size has been also carried out. Results have demonstrated that the effect of small changes in the grain shape is more important than the effect of the RVE size. It is shown that grain elastic anisotropy plays an important role in microfracture. Higher crack densities have been observed when grain elastic anisotropy is considered. In order to account for the fact that all the grain facets are not the same, due to grain misorientation and the presence of second phases, impurities and defects, the stochasticity of the microfracture process has been examined. Depending on which interface parameter is chosen to vary statistically, the crack density may or may not exceed the crack density if no variation is considered.

A study of grain size and shape reveals that crack density is strongly dependent on the grain shape. Decreasing the grain size results in a decrease in crack density per unit area at equal multiaxial dynamic loading.

The calculations in this article present assumptions that limit the degree of achievable accuracy. For instance, the calculations are 2-D instead of 3-D. As a result, a true random orientation of grains cannot be achieved in the representative volume element. In fact, in each grain one of the principal axis must always coincide with the global z axis. Moreover, crack interaction is stronger than in the 3-D case and therefore, the computed rate of crack coalescence may be thought of as an upper bound.

Another assumption employed in the case study of pressure-shear recovery experiment was the impossibility of sliding between the flyer–specimen and specimen–target interfaces. A more detailed calculation would require the modeling of anvil plates and the addition of roughness on the surfaces in contact. Furthermore, contact between surfaces should be implemented such that, in the presence of sliding, contact periodicity is achieved.

In the present analyses, the main damage and failure mode investigated was microcracking. However, in cases of stronger waves, visco–plasticity and twinning can be expected to become significant. Our model can account for visco–plasticity but further developments are required to model twinning. In this respect, continuum models of the type proposed by Staroselsky and Anand (1998) or the use of cohesive laws based on displacement jumps, e.g., law III in Espinosa et al. (2000b), seem promising approaches. Nonetheless, the physical modeling of coupled plasticity, twinning and microcracking continues to be challenging. In fact, it is known that twinning and/or dislocation pile ups are the precursors to microcrack initiation. To this picture it is necessary to add the stochasticity in grain boundary toughness due to the presence of thin (10 nanometers or less) glassy phase layers, grain boundaries with various values of coincident lattice sites, etc.

Future modeling work will attempt to include the features just discussed. The goal still being the development of models capable of predicting inelasticity in ceramic materials in a variety of quasi-static and dynamic applications.

Acknowledgements

H.D. Espinosa would like to thank J. Hutchinson for providing insight on the role of the cohesive law shape and parameters in the prediction of fragmentation. He also acknowledges the support from the Division of Engineering and Applied Sciences at Harvard University during his sabbatical visit. The authors acknowledge the discussion and collaboration provided by S. Dwivedi in the implementation of the computational model. They would also like to thank the ARO and DoD HPCMP for providing supercomputer time on the 128 processors Origin 2000 at the Naval Research Laboratory — DC (NRL–DC). This research was supported by the National Science Foundation through Career Award Nos. CMS 9523113, CMS–9624364, the Office of Naval Research YIP through Award No. N00014–97–1–0550, the Army

Research Office through ARO–MURI Award No. DAAH04–96–1–0331 and the Air Force Office of Scientific Research through Award No. F39620–98–1–0039.

References

Addessio, F.L., Johnson, J.N., 1989. A constitutive model for the dynamic response of brittle materials. LA–UR–89–2651, Los Alamos National Laboratory, Los Alamos, NM, USA.

Bolander, J., Saito, S., 1998. Fracture analyses using spring networks with random geometry. Engineering Fracture Mechanics 61, 569–591.

Bollmann, W., 1970. Crystal defects and crystalline interfaces. Springer-Verlag, Berlin.

Camacho, G.T., Ortiz, M., 1996. Computational modeling of impact damage in brittle materials. International Journal of Solids and Structures 33, 2899–2938.

Clifton, R.J., Klopp, 1985, 1985. Pressure–Shear Plate Impact Testing, Metals Handbook: Mechanical Testing, 8, 9th ed. Soc. Metals, Metals Park.

Curran, D., Seaman, L., Cooper, T., Shockey, D., 1990. Micromechanical model for comminution and granular flow of brittle material under high strain rate application to penetration of ceramic targets. International Journal of Impact Engineering 13, 53–83.

Espinosa, H.D., Raiser, G., Clifton, R.J., Ortiz, M., 1992. Performance of the star-shape flyer in the study of brittle materials: Three dimensional computer simulations and experimental observations. Journal of Applied Physics 72, 3451–3457.

Espinosa, H.D., 1995. On the dynamic shear resistance of ceramic composites and its dependence on applied multiaxial deformation. International Journal of Solids and Structures 32, 3105.

Espinosa, H.D., 1992, Micromechanics of the dynamic response of ceramics and ceramic composites. Ph.D Thesis, Brown University.

Espinosa, H., Zavattieri, P., Emore, G., 1998a. Adaptive FEM Computation of geometric and material nonlinearities with application to brittle failure. Mechanics of Materials 29, 275–305.

Espinosa, H., Zavattieri, P., Dwivedi, S., 1998b. A finite deformation continuum/discrete model for the description of fragmentation and damage in brittle materials. Journal of the Mechanics and Physics of Solids 46 (10), 1909–1942.

Espinosa, H., Patanella, A., Xu Y., 2000a. Pressure–shear soft recovery experiments. Experimental Mechanics (submitted).

Espinosa, H.D., Dwivedi, S., Lu, H.-C., 2000b. Modeling impact induced delamination of woven fiber reinforcer composites with contact/cohesive laws. Computer Methods in Applied Mechanics and Engineering, special issue (in press).

Ghosh, S., Yunshan, L., 1995. Voronoi cell finite element model based on micropolar theory of thermoelasticity for heterogeneous materials. International Journal of Numerical Methods and Engineering 38, 1361–1368.

Ghosh, S., Nowak, Z., Lee, K., 1997. Tessellation-based computational methods for the characterization and analysis of heterogeneous microstructures. Composite Science and Technology 57, 1187–1210.

Grah, M., Alzebdeh, K., Sheng, P., Vaudin, M., Bowman, K., Ostoja-Starzewki, M., 1996. Brittle intergranular failure in 2D microstructures: experiments and computer simulations. Acta Materials 44 (10), 4003–4018.

Hearmon, R.F.S., 1956. The elastic constants of anisotropic materials II. Advances in Physics 5, 323–382.

Jiao, S., Jenkins, M., Davidge, R., 1997. Interfacial fracture energy-mechanical behavior relationship in Al_sO_3/SiC and Al_sO_3/TiN Nanocomposibes. Acta Materials 45 (1), 149–156.

Johnson, G.R., Holmquist, T.J., 1992. A computational constitutive model for brittle materials subjected to large strains, high strain rates and high pressures. In: Meyers, M.A., Murr, L.E., Staudhammer, K.P. (Eds.), Shock-Wave and High Strain Rate Phenomena in Materials. Marcel Dekker, New York, p. 1075.

Kim, B.-N., Wakayama, S., Kawahara, M., 1996. Characterization of 2-dimensional crack propagation behavior by simulation and analysis. International Journal of Fracture 75, 247–259.

Lin, H.-T., Alexander, K., Becher, P., 1996. Grain size effect, on creep deformation of alumina–silicon carbide composites. Journal of the American Ceramics Society 79 (6), 1530–1536.

Liu, Y., Kegayama, Y., Murakami, S., 1998. Creep fracture modeling by use of continuum damage variable based on Voronoi simulation of grain boundary cavity. International Journal of the Mechancis of Science 40 (2/3), 147–158.

Luo, J., Stevens, R., 1997. The role of residual stress on the mechanical properties of Al_2O_3-5 Vol.% SiC nanocomposites. Journal of the European Ceramic Society 17, 1565–1572.

Miller, O., Freund, L.B., Needleman, A., 1999. Modeling and simulation of dynamic fragmentation in brittle materials. International Journal of Fracture 96 (2), 101–125.

Mullen, R.L., Ballarini, R., Yin, Y., Heuer, A., 1997. Monte carlo simulation of effective elastic constants of polycrystalline thin films. Acta Materials 45 (6), 2247–2255.

Onck, P., Van der Giessen, E., 1999. Growth of an initially sharp crack by grain boundary cavitation. Mechanics and Physics of Solids 47, 99–139.

Ortiz, M., Pandolfi, A., 1999. Finite-deformation irreversible cohesive elements for three-dimensional crack-propagation analysis. International Journal for Numerical Methods in Engineering 44 (9), 1267–1282.

Ortiz, M., Suresh, S., 1993. Statistical properties of residual stresses and intergranular fracture in ceramic materials. Journal of Applied Mechanics 60, 77–88.

Staroselsky, A., Anand, L., 1998. Inelastic deformation of polycrystalline face centered cubic materials by slip and twinning. Journal of the Mechanics and Physics of Solids 46 (4), 671–696.

Sternitzke, M., 1997. Review: Structural ceramic nanocomposites. Journal of the European Ceramic Society 17, 1061–1082.

Simpson, Y., Carter, B., 1990. Faceting behavior of alumina in the presence of glass. Journal of the American Ceramics Society 73 (8), 2391–2398.

Tasker, P., Duffy, D., 1983. Computer simulation of $\langle 001 \rangle$ tilt, grain boundaries in nickel oxide. Philos Magazine 37 (A), L45.

Tvergaard, V., 1990. Effect of fibre debonding in a whisker-reinforced material. Materials Science and Engineering A125, 203.

Tvergaard, V., Hutchinson, J., 1988. Microcracking in ceramics induced by thermal expansion or elastic anisotropy. Journal of the American Ceramics Society 71 (3), 157–166.

Underwood, E.E., 1970. Quantitative Stereology. Addison-Wesley, Reading, MA.

Weibull, W., Sweden, S., 1951. A statistical distribution function of wide applicability. Journal of Applied Mechanics 18, 293–297.

Wolf, D., 1984. On the relationship between symmetrical tilt, special, and favored, grain boundaries. Journal de Physique 4 (46), C4–197.

Wu, M., Niu, J., 1995a. Micromechanical prediction of the compressive failure of ice: model development. Mechanics of Materials 20, 9–32.

Wu, M., Niu, J., 1995b. Micromechanical prediction of the compressive failure of ice: numerical simulations. Mechanics of Materials 20, 33–58.

Xu, X.-P., Needleman, A., 1995. Numerical simulation of dynamic interfacial crack growth allowing for crack growth away from the bond line. International Journal of Fracture 74, 253–275.

Zhou, M., Needleman, A., Clifton, R.J., 1994. Finite element, simulations of shear localization in plate impact. Journal of the Mechanics and Physics of Solids 42 (3), 423–458.